Polymorphic Metastability in Colloidal Semiconductor Nanocrystals

Bryce A. Tappan and Richard L. Brutchey*

Department of Chemistry, University of Southern California, Los Angeles, California 90089, United States

Abstract: Metastable polymorphs of inorganic solids often possess material properties not present in the corresponding thermodynamic polymorphs, making them targets for the development of new functional materials. In contrast with isolating metastable bulk materials, syntheses of metastable polymorphs on the nanoscale are aided by fast non-equilibrium reaction kinetics and the favorable thermodynamic influence of surface energies, giving rise to greater ease of access to metastable high-temperature polymorphs and, in some cases, new polymorphs that do not exist in the bulk. The syntheses of metastable semiconductor nanocrystals are of interest for their potentially unique optoelectronic and physicochemical properties. However, in many material systems, synthesizing nanocrystalline products away from thermodynamic equilibrium in a predictable manner remains an outstanding challenge. This review outlines direct synthetic methodologies that have been developed to enable control over the nucleation and growth of metastable polymorphs of semiconductor nanocrystals by tailoring reaction conditions, precursor kinetics, ligand and surface effects, and other synthetic levers. The case studies reviewed herein expound on the direct syntheses of metastable ZnSe, Cu_2SnSe_3, $CuInSe_2$, Ag_2Se, and $AgInSe_2$ nanocrystals, and although there remain numerous examples of metastable nanocrystal syntheses outside of these metal chalcogenide systems, the concepts discussed are of general utility to the field of metastable nanocrystal syntheses as a whole. Explicit examples in which new functional properties are afforded by metastable polymorphs of the aforementioned material systems are presented within the context of applications for solar cells, photonics, and optical sensing. Finally, the factors that affect the kinetic persistence of metastable nanocrystalline polymorphs are discussed at length for these material systems.

1. Introduction

Metastability in colloidal nanocrystals manifests in many ways. Nanocrystal morphologies, sizes, compositions, and crystal structures can all exhibit different forms of metastability. Due to the diverse nature of metastability in colloidal nanocrystals, this review will be limited to the syntheses, properties, and applications of metal chalcogenide semiconductor nanocrystals that crystallize in metastable crystal structures. Before these specific chemistries are highlighted, we will introduce important concepts and terminology that will be used throughout this review by using a canonical example — the polymorphic metastability of the diamond allotrope of carbon.

Diamond is one of the two crystalline structures, or *polymorphs*, that elemental carbon adopts as a bulk material, and it represents the thermodynamically most stable polymorph of carbon only at pressures on the order of $P > 10^4$ atm.[1] Below these pressures, diamond has a free energy higher than the graphite polymorph of carbon, and therefore it is referred to as *metastable* with respect to graphite. Here, the term 'metastable' indicates only the relative thermodynamic stabilities between these two polymorphs; that is, it does not describe the timescale over which diamond will spontaneously convert to graphite. As a metastable polymorph of carbon, diamond is temporally *persistent* over long time scales due to the large activation energy barrier (from the required cleavage of sp^3 C-C bonds) that must be overcome for the reconstructive transformation of diamond into graphite.[2]

Humans have had a fascination with diamond dating back to antiquity. Diamond is an exceptional material – it has the greatest atom density of all terrestrial materials, is the hardest naturally occurring substance, and it has the highest room-temperature thermal conductivity of any material.[3] In addition, diamond is optically transparent through a wide range of wavelengths from the infrared to the ultraviolet region of the electromagnetic spectrum.[3] Graphite, the thermodynamic polymorph of carbon at low pressures, does not exhibit any of these same properties. The dichotomy between graphite and diamond exemplifies how the crystal structure of a material dictates its properties and is illustrative of the drastic property differences that can arise between metastable and thermodynamic polymorphs of a material with a fixed composition.

Polymorphism is pervasive in the chemistries of colloidal semiconductor nanocrystals. Herein, we discuss the state of the art regarding the direct syntheses of metastable polymorphs of metal chalcogenide semiconductor nanocrystals, with some of these polymorphs being previously unknown for the bulk materials. Then, we will highlight properties that these metastable polymorphs exhibit in comparison to their thermodynamically preferred counterparts, including examples in which the emergent properties of metastable semiconductor nanocrystals have been leveraged to improve applications in photonics, optical sensing and imaging, and solar cells.

2. Syntheses of Colloidal Semiconductor Nanocrystals with Metastable Crystal Structures

Metastable materials can have strikingly unique properties that are quite distinct from their thermodynamic counterparts. Unfortunately, metastable inorganic materials, such as diamond, have historically proven difficult to synthesize.[1,2,4,5] However, polymorphic metastability is much more prevalent on the nanoscale than for bulk materials. For colloidal nanocrystals, the surface energy (γA, where γ = interfacial excess free energy and A = interfacial area of the nanocrystal) represents a significant thermodynamic contribution to the relative stabilities between different crystalline phases.[6–8] This term scales with the surface area to volume ratio (A/V) and becomes an increasingly more dominant factor for nanocrystals of smaller sizes, or volumes. These surface energy contributions can compress differences in free energy between polymorphs, as compared to the bulk, and in some cases can even cause shifts in the ordering of the thermodynamic stabilities of polymorphs for a given material.[6,7,9–11]

Reductions in free energy differences between polymorphs and the fast reaction kinetics of nanocrystal nucleation and growth make it possible to synthesize colloidal nanocrystals with metastable crystal structures that in bulk are only accessible at much higher temperatures than those required for the analogous nanocrystal syntheses.[12] In addition to nanocrystalline analogues of bulk materials, entirely new crystal phases can also arise on the nanoscale that have no bulk counterparts.[13–23] Therefore, colloidal nanocrystal chemistry presents both thermodynamic and kinetic advantages in the preparation of metastable materials, and promises to be fruitful for the discovery of new metastable materials with unique properties. That said, we generally lack synthetic principles that enable chemists to predictably isolate novel nanomaterials with metastable crystal structures. Many of the metastable nanomaterials isolated thus far were done so serendipitously, and ab initio prediction of these phases is difficult, especially when there is no bulk analogue to suggest that such phases should exist on the nanoscale.[24]

Of the synthetic techniques employed to generate metastable polymorphs of semiconductor nanocrystals, cation exchange is the most well-understood framework to date. In the syntheses of bulk inorganic solids, high temperatures are generally needed to overcome the sluggish kinetics associated with solid-solid diffusion, making the isolation of metastable species challenging, as these synthetic conditions almost invariably favor the formation of thermodynamic products.[25,26] On the nanoscale, however, cation exchange can readily occur in inorganic nanocrystals. At this length scale, fast reaction kinetics are in part the result of the inherently high surface area-to-volume ratios of nanomaterials, resulting in drastic reductions of ion diffusion lengths through the solid and a high proportion of defects and vacancies, which also increase cation exchange rates.[27] Additionally, the organic ligands present in these syntheses facilitate the exchange of ions at the organic/inorganic interface of nanomaterials.[12,28–30] Cation exchange reactions are characterized by the complete or partial exchange of cations within a nanostructure in such a way that the overall particle morphology and the anionic sub-lattice of the nanostructure remain intact.[31–33] While sulfides and selenides are the most widely studied material systems for cation exchange reactions, this method has been used to synthesize a broad range of nanocrystalline compounds, many with metastable crystal structures. Indeed, cation exchange has been applied to the syntheses metal chalcogenides (for oxides, sulfides, selenides, and tellurides), metal pnictides (for phosphides and antimonides), and metal fluorides.[29,34] While cation exchange has proven to be a widely used method for the syntheses of novel metastable nanomaterials, there is a wide body of cation exchange literature and the topic has already been reviewed.[28,29,34,35] Therefore, we will focus on the direct syntheses of nanocrystals with metastable crystal structures and will only discuss cation exchange within the context of mechanisms of direct nanocrystal syntheses.

Direct methods, such as hot-injection or heating-up procedures, are beneficial in that they do not require multiple steps and/or post-synthetic modifications to yield the desired material. Even so, direct syntheses of metastable polymorphs of semiconductor nanocrystals remain an outstanding challenge due to the necessity of tuning precursor reactivities, which are often solvent-dependent, in addition to optimizing the time, temperature, and other experimental parameters to yield conditions that result in preferential nucleation and growth of metastable polymorphs.[34,36–38] In most cases, the effects of these variables (and their interactions) are complex and therefore still poorly understood.[39,40] In the following section, we review examples of direct syntheses of semiconductor nanocrystals with metastable crystal structures. While there are numerous reports of the syntheses of different polymorphs for many material systems, we review the work that provides insight into the factors that determine control over the crystalline phase of the products. We will identify advances that have led to increased predictability of reaction products, as well as areas that warrant further investigation.

2.1 Nanocrystal Polymorph Dependence on Reaction Conditions

2.1.1 Phase Control of ZnSe Nanocrystals via Modulation of Rate of Precursor Addition

ZnSe, a wide band gap II-VI semiconductor (bulk band gap, $E_g = 2.7$ eV), is an important phosphor material that emits in the blue to ultraviolet region of the electromagnetic spectrum, making it useful for applications in blue light emitting diodes (LEDs) and laser diodes.[41–43] Zunger et al. found that for binary octet semiconductors, the zinc blende structure is increasingly more stable than the wurtzite structure as the atomic number of the anion increases, progressing down a group in the periodic table. They coined this trend the "anion rule" of wurtzite-zinc blende polymorphism.[44] As predicted by the anion rule, bulk ZnSe is thermodynamically stable at low temperatures in the cubic zinc blende phase. Above 1411 °C, ZnSe undergoes a first-order phase transformation to the hexagonal wurtzite structure, which is stable up to the melting point of 1522 °C.[45] The zinc blende and wurtzite structures are polytypes of each other, meaning their structures have the same periodicity in two dimensions but differ in periodicity along one crystallographic direction.[46] This can be seen in **Figure 1**, where the wurtzite structure exhibits ABAB packing along the *c*-direction, leading to an eclipsed dihedral conformation, while the zinc blende structure packs in an ABCABC fashion and produces a staggered dihedral conformation.[44]

Polytypism is a common form of polymorphism and results in structures that are often narrowly separated from one another in terms of their thermodynamic stabilities. For ZnSe, the calculated total energy difference between these two polytypes reveals that the zinc blende structure is a mere 5.3 meV/atom more stable than the wurtzite structure (at 0 K);[44] 5.3 meV/atom is only 20% of kT at 298 K. This low energy threshold between these two phases means that, on the nanoscale, formation of either phase can be favored depending on the synthetic conditions.

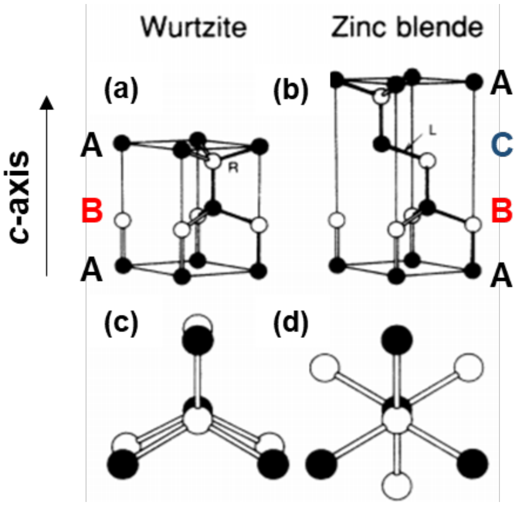

Figure 1. (a) and (b) show the difference in packing along the *c*-axis for the wurtzite and zinc blende structures, respectively. (c) and (d) highlight the fact that the wurtzite structure has an eclipsed dihedral conformation while the zinc blende structure has a staggered dihedral conformation. Adapted with permission from reference [44]. Copyright 1992, American Physical Society.

In a relatively early example of rational phase control, Cozzoli et al. demonstrated control over the phase and morphologies of ZnSe nanocrystals by modulating the conditions of nanocrystal nucleation and growth.[8] Here, the direct syntheses of ZnSe nanocrystals were performed by injecting precursor solutions containing diethyl zinc and trialkylphosphine-selenium adducts into a hot alkyamine solvent. Control over the phase and morphologies of the resultant nanocrystals was achieved by varying the reaction times, temperatures, volumes/concentrations, and rates of precursor addition.

A fast injection of the Zn/Se precursor solution promoted nucleation of isotropic ZnSe nanocrystals in the zinc blende phase (**Figure 2a**). For these reactions, the initial temperature of the alkylamine solvent was maintained at or above 300 °C. Following injection of the precursor solution, the reaction solution temperature fell to ~265 °C and was kept at that temperature for the remainder of the reaction. At this lower temperature, additional precursor solution was injected into the reaction flask dropwise (0.2 mL min^{-1}) over 3-5 h to facilitate further growth of the ZnSe nanocrystals, ultimately resulting in relatively monodisperse zinc blende nanocrystals 3-5 nm in diameter (**Figure 2b**). The hot-injection method enables temporal separation of the nanocrystal nucleation and growth processes; the initial high temperature of the alkylamine solvent is sufficient to overcome the activation

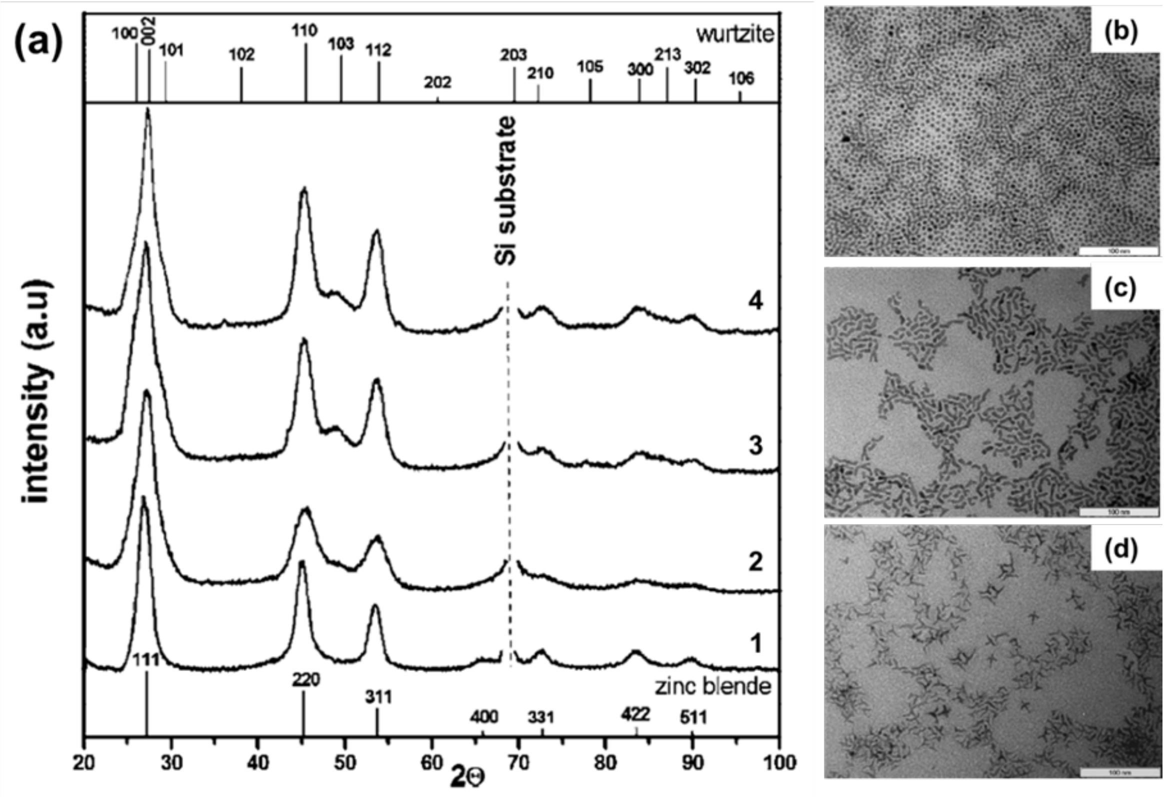

Figure 2. (a) Powder X-ray diffraction (XRD) of ZnSe nanocrystals; pattern **1** corresponds to spherical zinc blende nanocrystals and patterns **2-4** correspond to ZnSe nanorods with aspect ratios of 3, 6, and 8, respectively. (b) Transmission electron micrographs (TEM) of isotropic zinc blende ZnSe nanocrystals. (c) TEM of ZnSe nanorods. (d) TEM of ZnSe multipods. All scale bars shown represent 100 nm. Adapted with permission from reference [8]. Copyright 2005, American Chemical Society.

energy barrier associated with nanocrystal nucleation. The subsequent drop in temperature of the reaction solution that follows injection restricts further nucleation events, and monomer conversion is steered towards promoting growth of the pre-existing nuclei, which is a kinetically faster process with a lower activation energy barrier than nucleation.[47]

To synthesize anisotropic ZnSe nanocrystals that exhibit the wurtzite structure, the Zn/Se precursor solution was added to the hot alkylamine solvent at a much lower rate using a syringe pump. It was shown that the rate of addition, the concentration/total volume of precursor solution, and the temperature of the receiving flask could all influence nanocrystal phase and morphology. At 345 °C, dropwise addition rates of the Zn/Se precursor solution ranging from 0.05-0.20 mL min^{-1} produced anisotropic wurtzite ZnSe nanorods (**Figure 2a,c**). Decreasing the temperature of the reaction flask by 15-55 °C while increasing the injection rate to 0.30-0.40 mL min^{-1} resulted in branched ZnSe multipods that contained both wurtzite and zinc blende domains (**Figure 2d**).

To rationalize these results, the authors posit that the chemical potential of the monomers in solution are vastly different between the hot-injection and dropwise addition methods. For the former, a high chemical potential is created since monomer supersaturation results as soon as the entirety of the precursor solution is quickly injected into the reaction flask — favoring fast, isotropic nucleation and growth in the zinc blende phase, which does not have a preferred growth axis.

In contrast, low monomer concentration was found to be a critical requirement for the nucleation and growth of wurtzite nanorods. Under low-concentration conditions, where precursors are added dropwise, monomer supersaturation does not occur quickly and therefore does not force immediate nucleation and growth of nanocrystals, allowing the system to reach a quasi-equilibrium between monomers in solution and nanocrystal nuclei before extensive nanocrystal growth occurs.

The fact that the dropwise method, which favors thermodynamic control rather than kinetic control, promoted nucleation and growth of wurtzite ZnSe nanorods is particularly interesting, because it indicates a possible reversal of the thermodynamic stabilities of the zinc blende and wurtzite polytypes under these conditions. This reversal may be a result of more favorable surfactant stabilization of nanocrystal surfaces in the wurtzite phase than the zinc blende phase, since the most prevalent facets (and therefore the most stable facets with the lowest surface energy) of the wurtzite nanorods observed by high-resolution TEM (HR-TEM) were the nonpolar (100) and (110) facets, which have no equivalent in the zinc blende structure.[8,48] Indeed, surface ligands have been shown to differentiate the formation of the zinc blende and wurtzite polytypes in related material systems, such as CdSe nanocrystals.[49]

The formation of ZnSe multipods, with both wurtzite and zinc blende domains, resulted primarily under conditions that strike a balance between thermodynamic and kinetic control. Lower temperatures, higher precursor volumes or concentrations, and slightly higher rates of precursor addition favor the kinetic formation of zinc blende nuclei, which could then support anisotropic growth of wurtzite-phase arms from the polar (111) terminated facets of zinc blende, which is atomically identical to the (001) plane of the wurtzite structure.[8,50] The main findings of this work underscore the ways in which the kinetics and thermodynamics of nanocrystal synthesis can be rationally manipulated by changing something as simple as the rate of precursor addition. By simultaneously pulling other synthetic levers, such as temperature and precursor concentrations, a high degree of control can be achieved to yield ZnSe nanocrystals with controlled phase and morphology.

2.1.2 Temperature-Dependent Phase Control of Cu_2SnSe_3 Nanocrystals

Copper tin selenides are an attractive class of materials as earth abundant, low toxicity semiconductors for photovoltaic devices.[51–53] At room temperature, bulk Cu_2SnSe_3 crystallizes with a monoclinic unit cell in which the cations assume specific positions within the unit cell. This monoclinic structure is derived from a distorted diamondoid zinc blende structure. At higher temperatures, entropic stabilization favors randomization of the cations within the unit cell; here, Cu_2SnSe_3 adopts the true zinc blende structure (space group $F\bar{4}3m$).[52,54]

In 2012, our group discovered that Cu_2SnSe_3 can crystallize in a wurtzite-like structure on the nanoscale, which is nonexistent on the bulk phase diagram.[21] Expanding upon this discovery, Ryan et al. demonstrated how phase control could be achieved within this system by leveraging different reaction temperatures and precursors.[51] In a typical synthesis for wurtzite-like Cu_2SnSe_3 nanocrystals, diphenyl diselenide (Ph_2Se_2), $Cu(oleate)_2$, and oleylamine were placed in a flask together and heated. Upon reaching 230 °C, $Sn(OAc)_4$ in oleylamine was injected and the reaction flask was allowed to recover to a reaction temperature of 240 °C for 30-60 min. This procedure resulted in fairly monodisperse wurtzite-like nanocrystals 26 nm in diameter (**Figure 3a-c**).

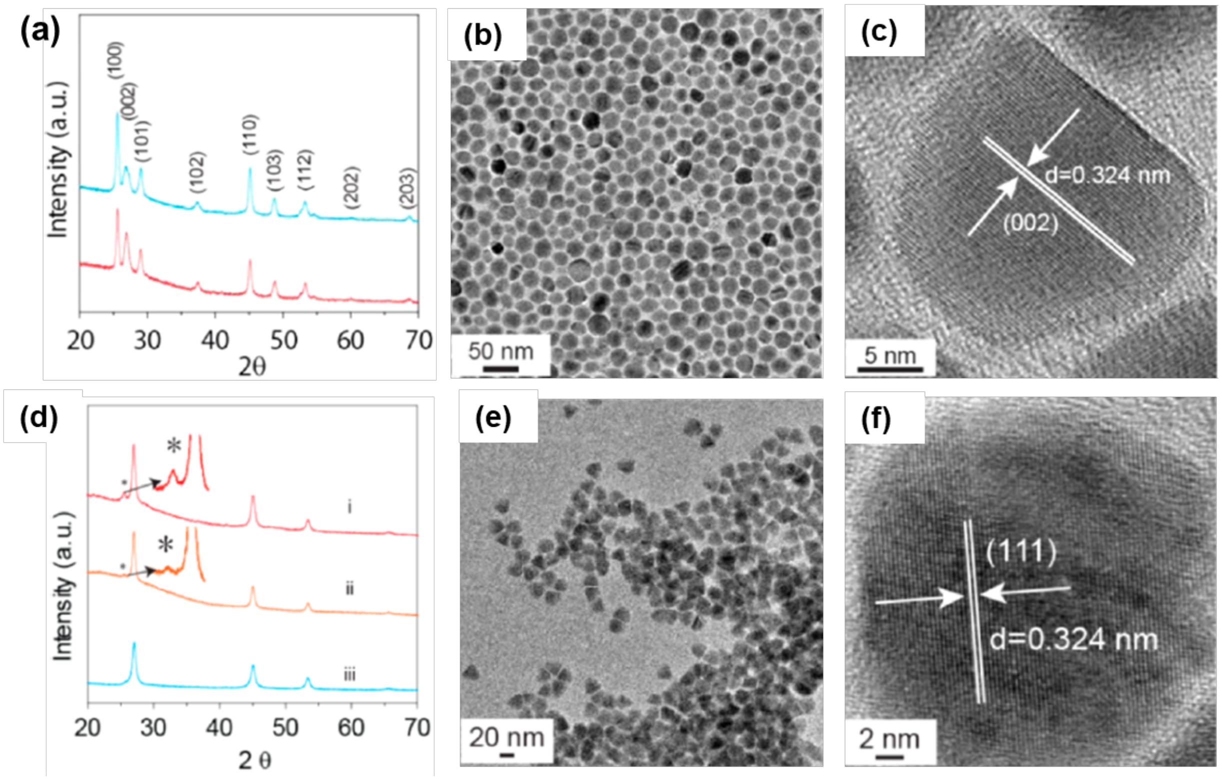

Figure 3. (a) Powder XRD patterns and (b,c) TEM and HR-TEM micrographs, respectively, of wurtzite-like Cu_2SnSe_3 nanocrystals synthesized from a hot-injection method at 240 °C. (d) Powder XRD patterns of zinc blende Cu_2SnSe_3 nanocrystals synthesized from hot-injection reactions using (**i-ii**) Ph_2Se_2 and (**iii**) Se powder. Note that patterns **i-ii** contain a small amount of the wurtzite-like phase, marked by an asterisk. (e,f) TEM and HR-TEM micrographs, respectively, of zinc blende nanocrystals synthesized with Ph_2Se_2. Adapted with permission from reference [51]. Copyright 2014, American Chemical Society.

By increasing the reaction temperature (and temperature of injection) to 300 °C, and using CuCl and $SnCl_2$ as metal precursors, nearly phase-pure zinc blende Cu_2SnSe_3 nanocrystals resulted (**Figure 3d-f**). Under these conditions, a small number of wurtzite-like nanocrystals remained, as evidenced by the presence of the (100) reflection from the wurtzite-like structure in the powder XRD pattern (**Figure 3d**). Even so, these experiments demonstrate the drastic influence temperature and precursor selection can have on phase determination, where near-complete phase control could be achieved by modulating the reaction temperature through a window of 60 °C. Additionally, these results reflect the metastability of the wurtzite-like phase with respect to the zinc blende phase for this ternary system, as the latter is favored under thermodynamically controlled conditions (i.e., high temperatures). Interestingly, when Ph_2Se_2 was used as a chalcogen source, no conditions were found under which Cu_2SnSe_3 could be isolated purely in the zinc blende phase. To eliminate all traces of the wurtzite-like phase, Ph_2Se_2 was replaced with elemental Se dissolved in oleylamine. Maintaining the relatively high reaction temperature of 300 °C with Se powder as the chalcogen source resolved this issue and yielded Cu_2SnSe_3 nanocrystals exclusively in the zinc blende phase (**Figure 3d**).

Ryan et al. were also able to synthesize Cu_2SnSe_3 polycrystalline tetrapods with domains of both the zinc blende and wurtzite-like structures in the same nanocrystal. To accomplish this, the synthetic conditions need to be such that one phase is favored during the nucleation stage and the other during the growth stage. To synthesize polytypic tetrapods, that is, tetrapods which contain both the zinc blende and wurtzite-like polytypes within the same nanostructure, the authors altered the original hot-injection synthesis for wurtzite-like Cu_2SnSe_3 by increasing the temperature of Ph_2Se_2 injection to 290 °C. In doing so, the initial high temperature of injection is sufficient to favor nucleation of small zinc blende seeds. However, the subsequent drop (~10 °C) in temperature that occurs following injection causes the kinetic growth of the wurtzite-like phase to dominate, allowing wurtzite-like arms to terminate four of the (111) facets of the zinc blende seed nanocrystals (**Figure 4a**).

The authors then demonstrated a complementary method of polytypic nanocrystal growth; that is, initial nucleation of hexagonal wurtzite-like seeds followed by epitaxial growth of the zinc blende phase. To do this, a heating-up method was employed whereby Ph_2Se_2, the metal precursors, and oleylamine were added to a single flask that was then ramped to 310 °C. While ramping, metastable wurtzite-like seeds nucleate at relatively lower temperatures, but as the temperature continues to rapidly increase, growth of the zinc blende phase becomes favored, generating linear nanostructures with a central wurtzite domain sandwiched by zinc blende domains along the tips of the nanocrystals (**Figure 4b**). In these experiments, it was found that final reaction temperatures exceeding 300 °C, and the use of CuCl and $SnCl_2$ chloride salts, were necessary to yield nanocrystals that uniformly exhibited such polytypism. Lower temperatures (280 °C), and the use of Ph_2Se_2 and $Cu(oleate)_2$ with $Sn(OAc)_4$, produced some heterostructures, but primarily resulted in phase-pure wurtzite-like nanocrystals, potentially due to the increased reactivity of the higher-valent Sn(IV) acetate precursor.

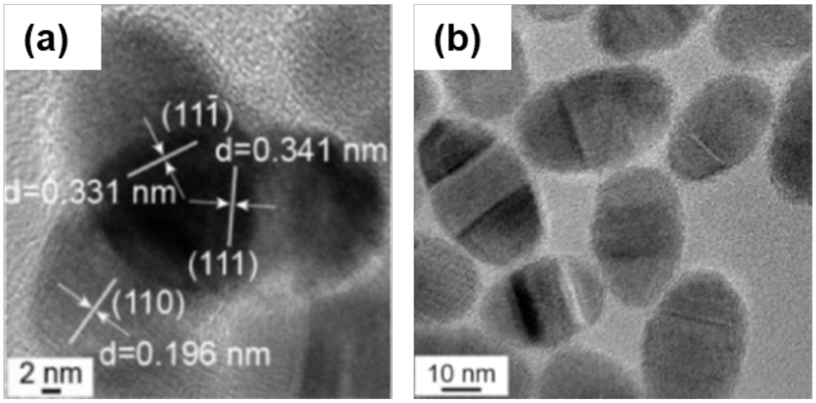

Figure 4. (a) TEM image of polytypic nanocrystalline tetrapods in which the arms are wurtzite-like and the central seed/core is zinc blende. (b) TEM image of polytypic linear nanocrystals in which the central domain/seed is wurtzite-like and the tips are zinc blende. Adapted with permission from reference [51]. Copyright 2014, American Chemical Society.

This work illustrates how temperature and precursor choice can be modulated to fine-tune the nucleation and growth kinetics of ternary semiconductor nanocrystals, where isolation of the metastable wurtzite-like phase can be obtained at relatively low temperatures with fast-reacting precursors. Thermodynamic control over the system can be achieved by increasing the overall reaction temperature by only 60 °C and by switching to less-reactive precursors. Manipulating the reaction conditions within the temperature window where kinetic and thermodynamic control compete can result in control over nanocrystal polytypism.

2.2 Tuning Precursor Reactivities for Polymorphic Phase Control on the Nanoscale

2.2.1 Polymorphic Control of $CuInSe_2$ Nanocrystals Using Diorganyl Dichalcogenides

Since the early 2000s, diorganyl dichalcogenides (R-E-E-R, where R = organic substituent and E = O, S, Se, Te) have emerged as increasingly useful molecular precursors for the syntheses of metal oxides and chalcogenides, especially metastable polymorphs of multinary metal chalcogenide nanocrystals.[20,21,23,55–59] This has already been introduced in the example of Cu_2SnSe_3 nanocrystals given above. Developing methods that afford fine control over the kinetics of nanocrystal nucleation and growth is crucial for the development of rational syntheses of new metastable polymorphs of semiconductor nanocrystals. One approach that has proven successful in controlling reaction kinetics is leveraging predictable trends in the reactivities of molecular precursors to affect the rates and/or conditions under which nanocrystal nucleation and growth occur.[60–62] In this regard, diorganyl dichalcogenides lend themselves to kinetically controlled syntheses, as their reactivities can be modulated by changing the identity of the organic substituent.[17,63–65] For example, in 2013, Vela et al. demonstrated that by changing the R group within a series of diorganyl disulfides or diselenides (R-S-S-R or R-Se-Se-R), they could tune the reactivities of these precursors as chalcogen sources in the preparation of CdS and CdSe nanocrystals, respectively. For each series, bond dissociation energies of the C-E and E-E bonds (E = S, Se) were calculated by density functional theory (DFT). While the strength of the E-E bonds was found to be relatively constant, the calculated C-E bond strengths change more dramatically upon substituting the R group, where precursors that possess large C-E bond dissociation energies are relatively less reactive compared to precursors with weaker C-E bonds. Experimentally, the more reactive dichalcogenide precursors yielded isotropic nanocrystals, whereas the less reactive precursors afforded anisotropic nanocrystals with higher surface areas, which are morphologically metastable with respect to isotropic nanocrystals with lower surface areas.[63]

In the last ten years, dichalcogenide precursors have been employed in the syntheses of ternary I-III-VI_2 semiconductor nanocrystals.[20,57,66,67] Ternary I-III-VI_2 semiconductor nanocrystals with an $A^{+}B^{3+}E^{2-}{}_2$ composition are of interest as relatively non-toxic alternatives to cadmium and lead-containing semiconductors, with applications in thin film solar cells, light emitting diodes (LEDs), photocatalysis, and bioimaging.[68] $CuInSe_2$ is a well-known I-III-VI_2 semiconductor, which, like other I-III-VI_2 semiconductors, crystallizes in the chalcopyrite structure (space group $I\bar{4}2d$) at low temperatures.[69] The tetragonal chalcopyrite structure type is characterized as a supercell of the zinc blende structure in which the anions pack in a face-centered cubic configuration while the cations fill 50% of the tetrahedral holes in an alternating fashion (**Figure 5c**).[69–71] At high temperatures, bulk $CuInSe_2$ assumes the zinc blende structure type up to its melting point, as shown in **Figure 5b**.[72–74] While bulk $CuInS_2$ behaves similarly in that it also undergoes a chalcopyrite-to-zinc blende phase transition with increasing temperature, a second high-temperature phase arises when heating the zinc blende phase beyond 1045 °C; namely, a wurtzite phase of $CuInS_2$ (**Figure 5a, 5c**), which is stable up to the melting point of 1090 °C.[75,76] Wurtzite $CuInS_2$ was also discovered to form on the nanoscale at reaction temperatures much lower than those necessary to achieve this phase in bulk.[77,78]

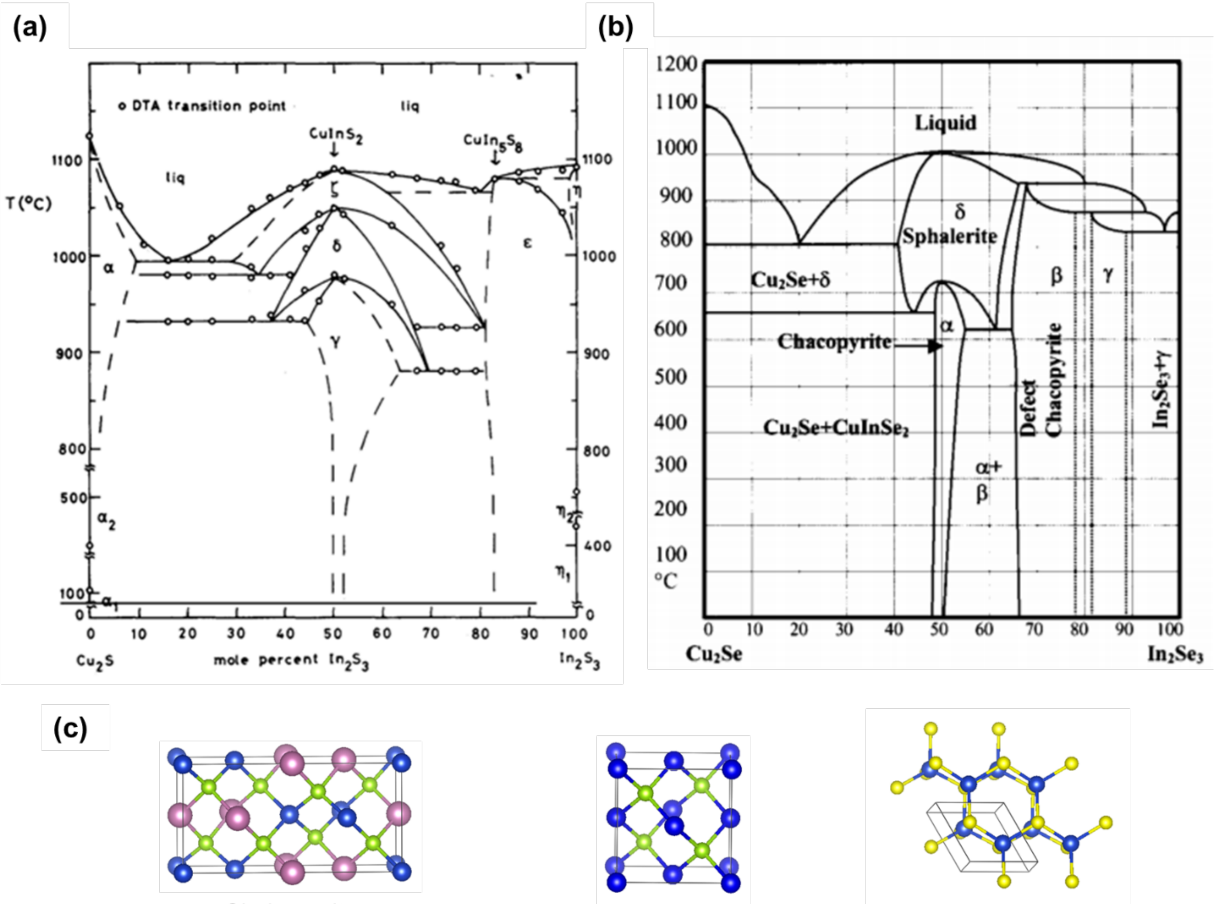

Chalcopyrite Zinc blende Wurtzite

Figure 5. (a) Cu_2S-In_2S_3 pseudo-binary phase diagram. Three phases of $CuInS_2$ exist in the bulk: the low-temperature chalcopyrite phase (labeled **γ**), a higher-temperature zinc blende phase (labeled **δ**), and the high-temperature wurtzite phase (labeled **ζ**). (b) Cu_2Se-In_2Se_3 pseudo-binary phase diagram. Two phases of $CuInSe_2$ exist in the bulk: the low-temperature chalcopyrite phase (labeled **α**), and the high-temperature zinc blende phase (also known as sphalerite, labeled **δ**). (c) Shown from left to right are the chalcopyrite structure type, the zinc blende structure type, and the wurtzite structure type for these ternary materials. For the chalcopyrite structure, blue atoms = Cu^+, pink atoms = In^{3+}, green atoms = S^{2-}/Se^{2-}. Note that the cations are ordered within the structure. For the zinc blende and wurtzite structure types, cations randomly occupy the tetrahedral holes, thus blue atoms represent both Cu^+ and In^{3+} in these structures, and green atoms = S^{2-}/Se^{2-}. Only $CuInS_2$ exhibits the wurtzite structure in bulk, so for this structure, yellow atoms = S^{2-}. Phase diagrams adapted with permission from reference [73], copyright 2000, AIP Publishing, and from reference [75], copyright 1980, Elsevier.

In 2010, we discovered that $CuInSe_2$ nanocrystals could be synthesized in a metastable wurtzite-like crystal structure, analogous to that of wurtzite $CuInS_2$, by using a Ph_2Se_2 diselenide precursor.[20] Here, we use the term "wurtzite-like" because these metastable hexagonal phases on the nanoscale often display long-range cation ordering within the crystal structures, whereas cations in the true wurtzite structure are not ordered.[79,80] Expanding upon the discovery of this new metastable phase of $CuInSe_2$, we hypothesized that trends in dichalcogenide precursor reactivity could be employed to control the reaction kinetics in the syntheses of $CuInSe_2$ nanocrystals, providing synthetic pathways for thermodynamically or kinetically driven mechanisms, thus enabling predictable phase control of this material system simply by changing the dichalcogenide precursor.

Diselenide precursors with different calculated C-Se bond strengths were used in the synthesis of the $CuInSe_2$ nanocrystals. To synthesize the nanocrystals, $InCl_3$ was hot-injected into a flask containing Cu(oleate)$_2$, a diselenide precursor, and oleylamine. **Figure 6** demonstrates that, when the diselenide precursors that possess stronger C-Se bond strengths (R = phenyl) were used, the resulting nanocrystals crystallize in a metastable wurtzite-like phase, whereas precursors with weaker C-Se bonds (R = methyl, benzyl) yielded the nanocrystals with the thermodynamic chalcopyrite crystal structure.[65] To confirm the dependence of the nanocrystalline phase on the C-Se bond strength, and not the Se-Se bond strength, benzeneselenol was employed as a selenium source. This precursor, which has a C-Se bond stronger than that of Ph_2Se_2 and no Se-Se bond, also produces the wurtzite-like phase, which provides further evidence that the C-Se bond strength is a primary phase-determining variable.

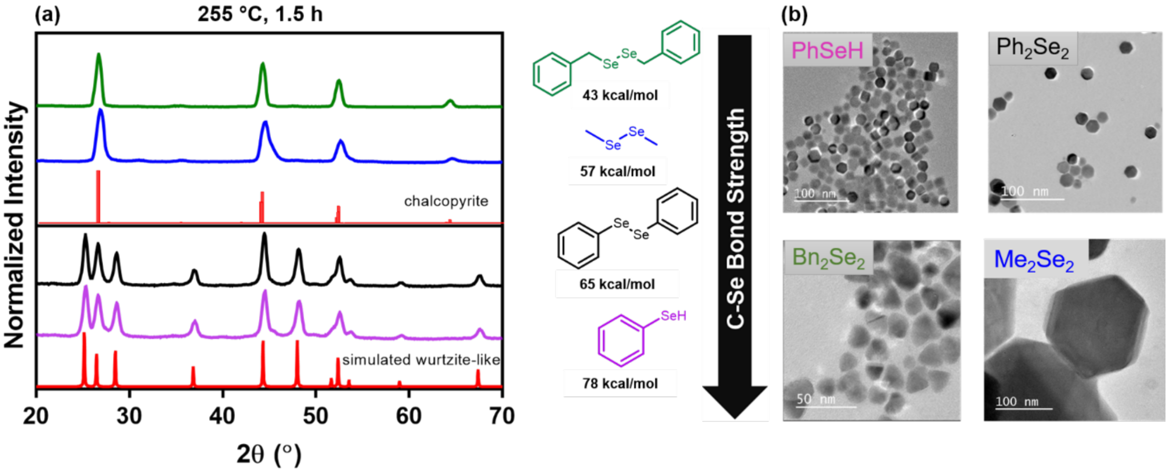

Figure 6. (a) Powder XRD patterns corresponding to $CuInSe_2$ nanocrystals synthesized with various diorganyl diselenide precursors. For R = benzyl and methyl, the resulting nanocrystals have the chalcopyrite structure, whereas for R = phenyl, the nanocrystals crystallize with a metastable wurtzite-like structure. (b) TEM micrographs of the $CuInSe_2$ nanocrystals derived from each respective precursor. Adapted with permission from reference [65]. Copyright 2018, American Chemical Society.

Ex situ aliquot studies by powder XRD revealed that each ternary polymorph arises from different distinct phases of binary copper selenide intermediates. Specifically, when using dimethyl or dibenzyl diselenide, the chalcopyrite phase is generated from an in-situ partial cation exchange reaction between cubic $Cu_{2-x}Se$ intermediates and In^{3+} in solution. This cation exchange is topotactic; the anion sub-lattice remains largely unchanged in transitioning from $Cu_{2-x}Se$ to chalcopyrite $CuInSe_2$.

In contrast, when Ph_2Se_2 was employed as the chalcogen source, the Cu_3Se_2 phase of copper selenide was observed as the sole intermediate that ultimately generates the wurtzite-like phase of $CuInSe_2$. Interestingly, Cu_3Se_2 is a low-temperature phase of copper selenide that is metastable at the temperatures of the hot-injection reaction.[81] By inspecting the crystal structure of Cu_3Se_2, we proposed a crystal chemistry mechanism that rationalizes the conversion of Cu_3Se_2 into wurtzite-like $CuInSe_2$. **Figure 7a, b** illustrates the near-isostructural relationship between the pseudo-hexagonal and hexagonal Se^{2-} sub-lattices of Cu_3Se_2 and wurtzite-like $CuInSe_2$, respectively. Thus, we hypothesized that the conversion of Cu_3Se_2 to wurtzite-like $CuInSe_2$ is also due to in-situ topotactic partial cation exchange with In^{3+}. To generate a wurtzite-like structure from Cu_3Se_2, the periodic tetrahedral holes within the structure (shown with dotted red lines in **Figure 7e**) must necessarily be filled by incoming In^{3+} atoms, or by Cu^+ atoms that migrate to accommodate In^{3+} in an identical tetrahedral hole elsewhere. To maintain charge balance during the cation exchange, the incoming In^{3+} cations must expel the equivalent of one Cu^+ cation and one Cu^{2+} cation, thus generating the $CuInSe_2$ composition. The most stable structure resulting from the exchange of two copper cations by an In^{3+} cation is that which is produced by the replacement of unfavorable, edge-sharing motifs in Cu_3Se_2 (highlighted in **Figure 7d**) with more favorable, corner-sharing motifs in the wurtzite-like structure (**Figure 7c**).

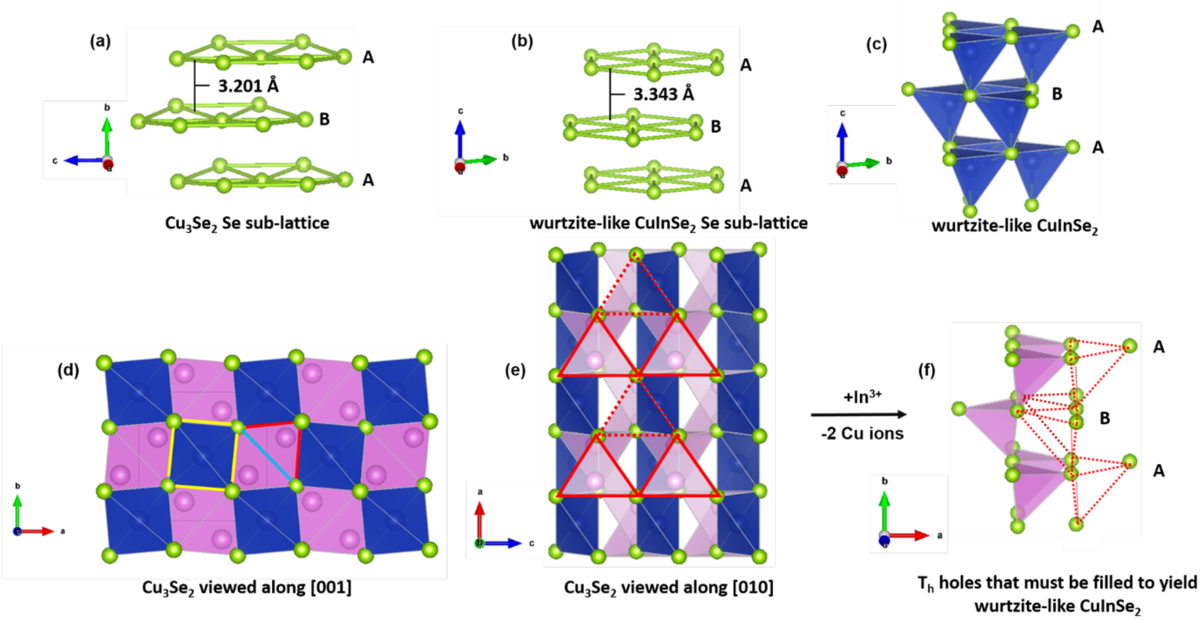

Figure 7. (a) Pseudo-hexagonal Se^{2-} sub-lattice of Cu_3Se_2. (b) Hexagonal Se^{2-} sub-lattice of $CuInSe_2$. (c) Wurtzite-like structure of $CuInSe_2$. (d) Side-view of Cu_3Se_2; edge-sharing configurations are highlighted in yellow, teal, and red. (e) Top-view of Cu_3Se_2; periodic tetrahedral holes within the structure are traced with dotted red lines. (f) Cu_3Se_2 structure visualized whereby all edge-sharing tetrahedra have been omitted and the periodic vacant tetrahedral holes in the structure have been traced with dotted red lines. This suggestive depiction of the Cu_3Se_2 structure appears nearly identical to the wurtzite structure shown in (c). In all structures, green = Se^{2-}. For the wurtzite-like structure, blue tetrahedra = Cu^+/In^{3+}. For the Cu_3Se_2 structures, pink and blue tetrahedra represent the two crystallographically unique copper sites within the crystal structure. Adapted with permission from reference [65]. Copyright 2018, American Chemical Society.

2.3 Ligand and Solvent Effects on Nanocrystal Polymorphism

2.3.1 Surface Stabilization of Metastable Ag_2Se Nanocrystals

Ag_2Se is a narrow-band gap semiconductor that can exhibit phase-dependent superionic Ag^+ conductivity and giant magnetoresistance.[82–85] In the bulk, Ag_2Se crystallizes in a low-symmetry orthorhombic phase up to ~135 °C, whereupon it undergoes a first-order phase transition to the superionic conducting body-centered cubic phase.[86–88] However, for nanocrystals, a third phase of Ag_2Se with tetragonal lattice parameters is also known to form at relatively low temperatures.[14–16,89,90] The crystal structure of this phase of Ag_2Se is unknown, as it is temporally and thermally metastable and only isolable when the crystallite size is confined to the nanoscale.[85] The complex interplay of phases on the nanoscale make Ag_2Se an intriguing and unique material system in the area of metastable nanocrystals.

The potential for coexistence of the orthorhombic, cubic, and tetragonal phases has led to a fair degree of confusion within the literature when providing phase assignments for Ag_2Se nanocrystals. This is largely due to the ease with which the unsolved tetragonal phase of Ag_2Se can be mistaken for orthorhombic Ag_2Se in powder XRD analysis. However, in recent years, synthetic methods have been developed to cleanly isolate the tetragonal phase of Ag_2Se independently of the other phases.[13,85,89,91] These studies have shown that the method of preparation of the tetragonal phase of Ag_2Se has profound effects on its properties and persistence.

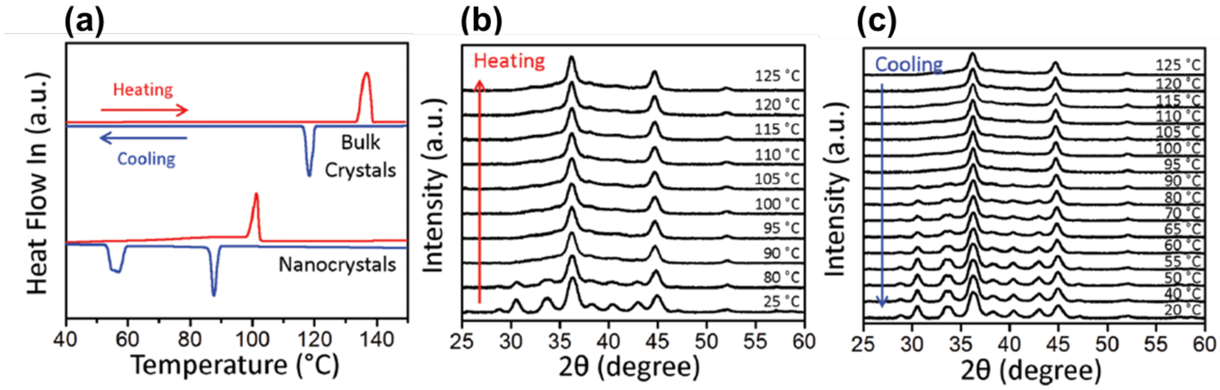

Figure 8. (a) Differential scanning calorimetry curves for tetragonal trioctylphosphine-stabilized Ag_2Se nanocrystals (bottom curve) and bulk Ag_2Se powder (top curve). (b) Heating and (c) cooling in variable-temperature powder XRD scans of 8.6 nm trioctylphosphine-stabilized tetragonal Ag_2Se nanocrystals. Adapted with permission from reference [85]. Copyright 2014, American Chemical Society.

The tetragonal phase has been shown to convert to cubic Ag_2Se upon heating. Cheng et al. and Norris et al. investigated the effect of the surface ligands on the temperature of this phase transition, demonstrating that surface stabilization with various *n*-alkylamines, trialkylphosphines, or polyvinyl pyrrolidone (PVP) all result in Ag_2Se nanocrystals capable of a reversible and direct tetragonal-to-cubic Ag_2Se phase transition around 101-109 °C (**Figure 8**).[13,85,91,92] When stabilized with PVP ligands, tetragonal Ag_2Se was found to be temporally stable for a week or longer at room temperature.[13] In contrast, it was found that tetragonal Ag_2Se nanocrystals exclusively stabilized with oleylamine ligands are much less thermally and temporally stable and do not exhibit the tetragonal-to-cubic phase transition. Upon heating, these nanocrystals undergo an exothermic, irreversible tetragonal-to-orthorhombic transition within a temperature range of 60-67 °C, and also revert to the orthorhombic phase of Ag_2Se after 8 h at room temperature.[13] Often, the physicochemical properties of nanomaterials are dependent on crystallite size. However, in this case, nanocrystal size does not explain the marked instability of tetragonal Ag_2Se prepared with oleylamine ligands, as the oleylamine-capped nanocrystals used in this study were of intermediate size (44 nm) compared to nanocrystals that displayed superior thermal and temporal stability (*n*-alkylamine or trialkylphosphine-capped nanocrystals were ~10 nm in diameter and the PVP-capped nanocrystals were ~125 nm in diameter).[13,85] Thus, for the oleylamine-stabilized nanocrystals, size effects do not account for the low-temperature tetragonal-to-orthorhombic phase transition.

Understanding the chemistry of the tetragonal Ag_2Se phase requires consideration of multiple interdependent factors, including the identity of the ligands, nanocrystal size, surface chemistry, and the influence of defects. As mentioned above, the tetragonal phase is only isolable for nanocrystals. In this regard, organic ligands are crucial in that they sterically prevent the agglomeration/sintering of the nanocrystals, enabling the persistence of the metastable phase on the nanoscale. In addition, surface ligands can selectively stabilize specific crystal facets, thereby influencing overall surface energy of the nanocrystals. Such ligand binding reduces the overall surface energy of the nanocrystals, and can favor the formation of a phase that is metastable (or nonexistent) in the bulk.[8,10,93] In seeking to explain the relative instability of the oleylamine-capped tetragonal Ag_2Se, Cheng et al. suggest that perhaps oleylamine stabilizes the nanocrystal surfaces less than the other ligands that were tested, giving rise to the unique low-temperature tetragonal-to-orthorhombic phase transition.[13] However, more studies are needed in order to fully understand why the oleylamine-capped tetragonal Ag_2Se behaves differently than Ag_2Se stabilized with other ligands.

2.3.2 Ligand-Mediated Phase Control of $AgInSe_2$ Nanocrystals

$AgInSe_2$ is a I-III-VI_2 semiconductor with a direct band gap and photoluminescence in the near-infrared region of the electromagnetic spectrum, making it potentially useful for near-infrared bioimaging.[94–99] As a I-III-VI_2 semiconductor, $AgInSe_2$ also crystallizes in the chalcopyrite structure type, as shown in **Figure 9a**, and region 12 of the phase diagram in **Figure 9c**.[100] On the pseudo-binary Ag_2Se-In_2Se_3 bulk phase diagram, chalcopyrite $AgInSe_2$ shows a relatively narrow tolerance for compositional deviations from the 1:1:2 ratio of Ag:In:Se. When heated past 963 K, a phase transition occurs in which the occupation of cation sites within the structure are randomized, leading to formation of a cubic zinc blende structure type with broader compositional tolerance (region 10 in **Figure 9c**).[101,102] A highly related system, $AgInS_2$, also crystallizes in the chalcopyrite structure at low temperatures, but adopts an orthorhombic wurtzite-like structure (space group $Pna2_1$, **Figure 9b**) at $T > 913$ K, as shown in **Figure 9d**;[103–105] this phase has also been isolated for $AgInS_2$ nanocrystals.[106] Interestingly, $AgInSe_2$ nanocrystals also can crystallize in an analogous orthorhombic structure, despite this phase not being present on the bulk phase diagram for $AgInSe_2$.[18,67,99,107–110]

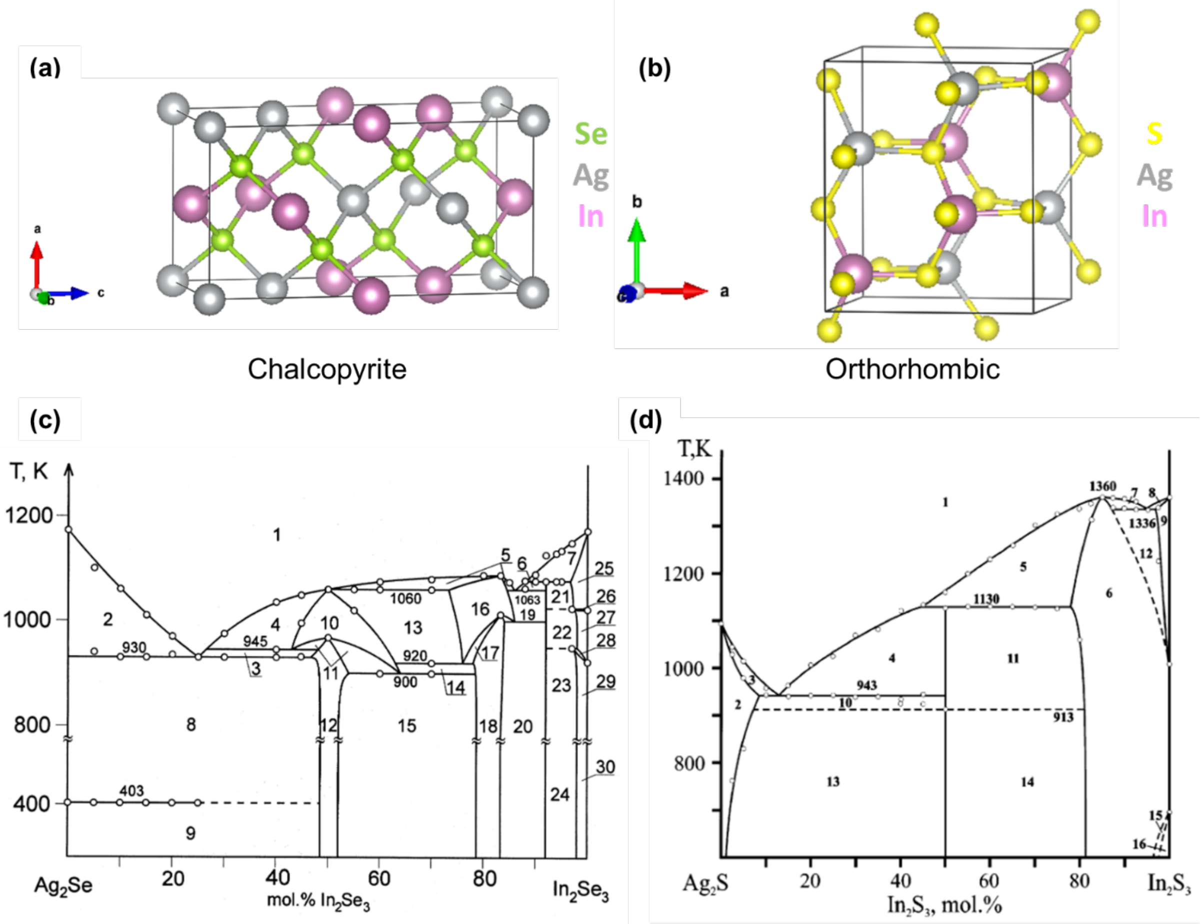

Figure 9. (a) Chalcopyrite structure of $AgInSe_2$. (b) Orthorhombic wurtzite-like structure of $AgInS_2$. For both structures, gray atoms = Ag^+, pink atoms = In^{3+}, green atoms = Se^{2-}, and yellow atoms = S^{2-}. (c) Pseudo-binary bulk phase diagram of the Ag_2Se-In_2Se_3 system. $AgInSe_2$ exists at the 50 mol%

composition. Regions **10**, **11**, and **12** represent $AgInSe_2$ with the zinc blende structure, zinc blende + chalcopyrite structures, and the chalcopyrite structure, respectively. The point at 1060 K between regions 1 and 10 lies on the liquidus curve and represents the melt temperature of $AgInSe_2$. (d) Pseudo-binary bulk phase diagram of the Ag_2S-In_2S_3 system. Region **5** = liquid + $AgIn_5S_8$, region **11** = orthorhombic $AgInS_2$ + $AgIn_5S_8$, region **14** = chalcopyrite $AgInS_2$. Phase diagrams adapted with permission from reference [101], copyright 2001, Elsevier, and reference [103], copyright 2008, Elsevier.

Recently, we showed that the judicious selection of coordinating ligands enables polymorphic control in the syntheses of $AgInSe_2$ nanocrystals.[67] In a general synthesis, the Ag^+ and In^{3+} precursors were dissolved together in a flask in either excess oleylamine or excess oleic acid. Then, the metal-containing flask was then heated and the Bn_2Se_2 solution was hot-injected into it at the desired temperature. When oleic acid is included as the coordinating ligand, the resulting $AgInSe_2$ nanocrystals crystallize in the thermodynamic chalcopyrite structure (**Figure 10a**), often with some Ag_2Se impurities (vide infra). In contrast, when oleylamine is used as the coordinating ligand, the $AgInSe_2$ nanocrystals exhibit the metastable orthorhombic structure (**Figure 10b**).

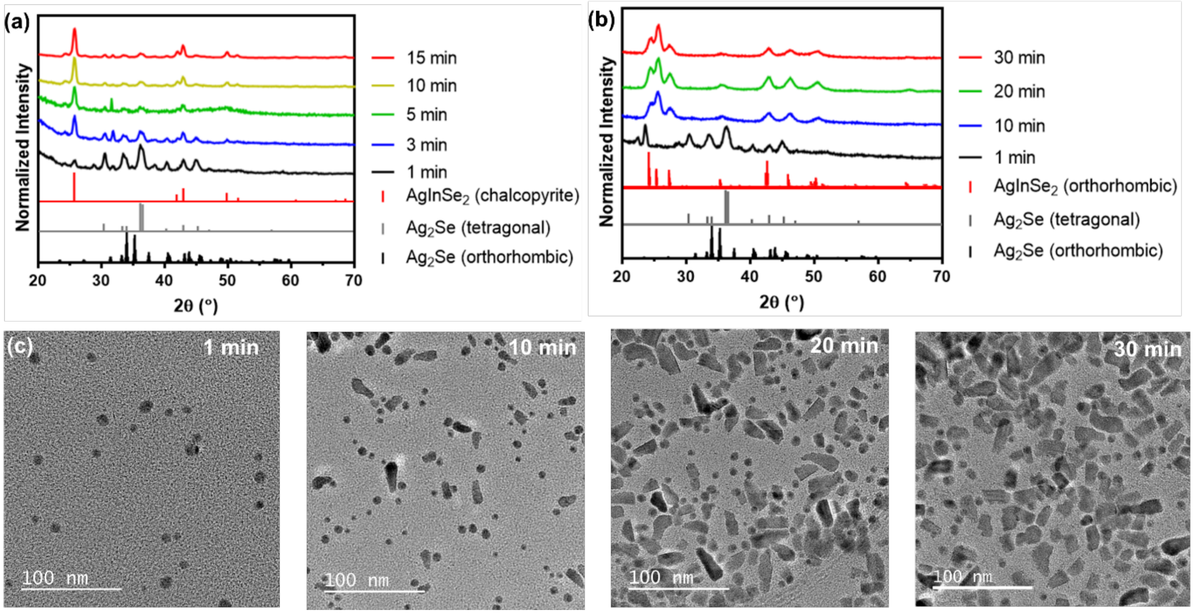

Figure 10. Powder XRD patterns corresponding to aliquots taken from reactions in which (a) oleic acid was employed as the coordinating ligand, and (b) oleylamine was employed as the coordinating ligand. (c) TEM micrographs corresponding to the XRD patterns shown in (b). Adapted with permission from reference [67]. Copyright 2020, American Chemical Society.

Ex situ powder XRD analysis of reaction aliquots provided insight into the reaction mechanism; in both cases, the aliquot taken 1 min after injection of Bn_2Se_2 revealed that binary Ag_2Se intermediates, namely, a mixture of orthorhombic and tetragonal Ag_2Se, form prior to formation of ternary $AgInSe_2$ nanocrystals. Although the initial Ag_2Se intermediates appear to be the same for the reactions containing oleic acid and oleylamine, later time points in the aliquot studies illustrate that these intermediates react in distinctly different ways, as the oleic acid reaction yields chalcopyrite $AgInSe_2$ and the oleylamine reaction yields orthorhombic $AgInSe_2$.

Although chalcopyrite $AgInSe_2$ nanocrystals represent the thermodynamic product for these reactions, generating this phase from binary Ag_2Se intermediates is kinetically slow, as none of the Ag_2Se intermediates are structurally similar to chalcopyrite. Orthorhombic Ag_2Se has a pseudo-hexagonal Se^{2-} sub-lattice (vide infra), whereas cubic Ag_2Se has a body-centered cubic Se^{2-} sub-lattice. The structure of tetragonal Ag_2Se is not known, but is thought to be derived from cubic Ag_2Se.[13,85] In contrast, chalcopyrite $AgInSe_2$ features a face-centered cubic Se^{2-} sub-lattice. Therefore, for any of these Ag_2Se intermediates to react with In^{3+} to yield chalcopyrite $AgInSe_2$, they must undergo a kinetically slow, reconstructive transition in which the anionic sub-lattices are disrupted and rearranged to produce a face-centered cubic structure. We believe it is this kinetic bottleneck that leads to the persistence of minor Ag_2Se impurities in the synthesis of chalcopyrite $AgInSe_2$ (**Figure 10a**).

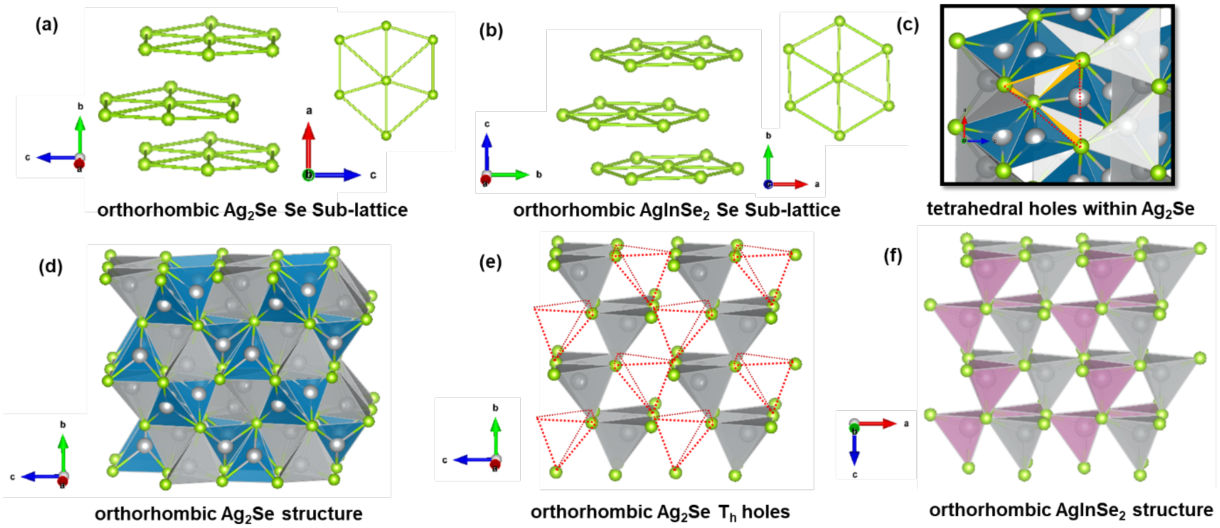

orthorhombic Ag_2Se Se Sub-lattice

orthorhombic $AgInSe_2$ Se Sub-lattice

tetrahedral holes within Ag_2Se

orthorhombic Ag_2Se structure

orthorhombic Ag_2Se T_h holes

orthorhombic $AgInSe_2$ structure

(all edge-sharing tetrahedra and trigonal planar coordination sites have been omitted)

Figure 11. (a) Pseudo-hexagonal Se^{2-} sub-lattice of orthorhombic Ag_2Se. (b) Hexagonal Se^{2-} sub-lattice of orthorhombic $AgInSe_2$. (c) Demarcation of the periodic tetrahedral holes in orthorhombic Ag_2Se. If this site was occupied with a cation, the resulting tetrahedron would be corner-sharing with neighboring tetrahedra along the edges highlighted in yellow. (d) Side-on view of orthorhombic Ag_2Se, with the two crystallographically unique Ag^+ sites shown in grey and blue. (e) Orthorhombic Ag_2Se when viewed by omitting all edge-sharing coordination sites while highlighting periodic tetrahedral holes within the structure with dotted red lines. (f) Orthorhombic $AgInSe_2$ structure; grey tetrahedra = Ag^+ sites, pink tetrahedra = In^{3+} sites, green atoms = Se^{2-}. Adapted with permission from reference [67]. Copyright 2020, American Chemical Society.

In contrast, we observed that the formation of phase-pure orthorhombic $AgInSe_2$ occurs quickly, as shown in **Figure 10b**. Several studies have reported the orthorhombic phase of Ag_2Se as an intermediate that precedes the metastable orthorhombic phase of $AgInSe_2$, although these reports did not elaborate on the mechanism of this transformation or the fate of tetragonal Ag_2Se in these reactions.[107–110] We proposed a mechanism whereby orthorhombic Ag_2Se converts directly to orthorhombic $AgInSe_2$ by an in-situ, ligand-mediated topotactic cation exchange process. **Figure 11** demonstrates the structural similarities between orthorhombic Ag_2Se and the metastable, orthorhombic phase of $AgInSe_2$. As can be seen by comparing **Figure 11a,b**, orthorhombic Ag_2Se possesses a nearly hexagonal Se^{2-} sub-lattice closely related to that found in orthorhombic $AgInSe_2$. Thus, we posited that a topotactic partial cation exchange process enables the transformation of the orthorhombic Ag_2Se, which contains edge-sharing Ag^+ polyhedral coordination environments, to orthorhombic $AgInSe_2$, which is characterized by having a more stable corner-sharing framework. Incoming In^{3+} cations fill the periodic tetrahedral holes (**Figure 11c, e**) that exist within the orthorhombic Ag_2Se structure, leading to the expulsion of three Ag^+ ions from two units of Ag_2Se to create the corner-sharing wurtzite-like structure shown in **Figure 11f**. Our proposed mechanism for this transformation is akin to the mechanism we proposed to explain the formation of metastable wurtzite-like $CuInSe_2$ from a copper selenide intermediate.[65] To account for the tetragonal Ag_2Se intermediate in this mechanism, we hypothesize that tetragonal Ag_2Se converts first to orthorhombic Ag_2Se, which can then undergo cation exchange to orthorhombic $AgInSe_2$.[67] Indeed, it is known that, when ligated with oleylamine, tetragonal Ag_2Se undergoes an irreversible phase transition to orthorhombic Ag_2Se at 60-67 °C.[13]

In the formation of chalcopyrite and orthorhombic $AgInSe_2$ nanocrystals, the kinetics of the evolution of the Ag_2Se intermediates depend upon the coordinating ligand present in the reaction mixture; reactions in which oleic acid is used yield chalcopyrite nanocrystals, while when oleylamine is used, orthorhombic nanocrystals result. Oleic acid is likely to take the form of oleate, an X-type ligand, which is a harder base than the neutral, L-type oleylamine ligand, and therefore not well-suited to mediate a fast topotactic cation exchange reaction by extracting soft Ag^+ cations from orthorhombic Ag_2Se intermediates. The kinetics of cation exchange reactions are largely dependent on metal-ligand interactions, which can be described using hard-soft acid base theory.[29] Thus, when oleate is present, the system proceeds down the slower, thermodynamic pathway characterized by a reconstructive reaction between Ag_2Se intermediates and In^{3+} to yield chalcopyrite $AgInSe_2$ nanocrystals. In contrast, the softer Lewis basic character of oleylamine matches the soft Ag^+ Lewis acid more appropriately, leading to a more favorable Lewis acid-base interaction and extraction of Ag^+ from orthorhombic Ag_2Se intermediates, allowing for a kinetically fast topotactic cation exchange process to outcompete the thermodynamic pathway for formation of $AgInSe_2$. Interestingly, quaternary $Cu_2ZnSnSe_4$ (CZTSe) nanocrystals exhibit a similar polymorphic dependence on the choice of ligand, demonstrating the generality of these synthetic strategies in preparing metastable polymorphs on the nanoscale.[23]

2.4 The Future of Metastable Nanocrystal Synthesis

While many of the first syntheses of nanomaterials with metastable crystal structures were discovered serendipitously, strategies are emerging that will galvanize the predictable syntheses of novel metastable polymorphs on the nanoscale. In addition to the synthetic techniques discussed above, computational methods have provided invaluable insight into factors that influence the "synthesizability" of metastable polymorphs. Thermodynamic considerations of phase stability allow prediction and experimental verification of the most stable polymorphs for material systems under certain conditions. However, any polymorph other than that defined by the thermodynamic structure for a given set of conditions is metastable, meaning that there is a seemingly infinite number of potential metastable phases for any material. Thus, evaluating the probability of the existence and potential for isolation of plausible polymorphs within a material system is an important, non-trivial task when seeking to synthesize novel metastable polymorphs.

In 2016, Cedar et al. conducted a data-mining study of DFT-calculated energies for nearly 30,000 inorganic compounds that appear within the Inorganic Crystal Structure Database (ICSD).[111] Of these compounds, roughly 50% were metastable. To complement the DFT calculations of these experimentally observed compounds, energy calculations were also carried out for hypothetical structures that were generated for different material systems by using an algorithm that makes chemically sensible compositional substitutions in existing crystal structures to create unobserved, but plausible, polymorphs in silico.

Figure 12a gives the probability densities of experimentally observed polymorphs (blue curve) and hypothetical metastable polymorphs (red curve) for binary metal oxides vs the energy of the respective metastable polymorphs. These curves demonstrate that energy above the thermodynamic ground state influences the likelihood of the existence of a metastable state. For the experimentally observed polymorphs, 90% of the metastable polymorphs were observed to be 94 meV/atom or less above the thermodynamic ground state, while the maximum probability for the energies of hypothetical, unobserved polymorphs was 150 meV/atom. This supports the intuitive notion that lower-energy metastable polymorphs are more likely to form than higher-energy polymorphs.

Importantly, energy above the ground state is not the sole predictor for synthesizability of metastable polymorphs. **Figure 12c** shows that, for these binary metal oxides, numerous hypothetical polymorphs that have never been experimentally observed have energies that are calculated to be less than the energies of experimentally observed polymorphs. To explain this phenomenon, Cedar et al. propose a concept of "remnant stability," whereby all isolable metastable polymorphs must be, under some set of thermodynamic conditions, the most stable polymorph. **Figure 12b** illustrates this idea, where the energy of an unobserved hypothetical metastable phase falls between the experimentally observed α and β phases for a given set of initial conditions. Manipulations of different thermodynamic parameters (temperature, pressure, etc.) stabilize the β phase with respect to both the α phase and the hypothetical metastable phase, allowing for isolation of the β phase under these new conditions. This example shows how, although the hypothetical metastable phase can have a relatively lower energy than the β phase under the initial conditions, it cannot be synthesized because it never represents the thermodynamically most stable state under any set of conditions.

Additionally, it was found that the range of energies of accessible metastable polymorphs tracks with the cohesive energy of the crystalline solids. For example, the median cohesive energy of chalcogenides follows the trend of oxides > sulfides > selenides > tellurides. Similarly, the range of energies of accessible metastable polymorphs above the thermodynamic ground state is greatest for oxides (0 – 100 meV/atom above ground state), followed by sulfides and selenides (0-75 meV/atom above the ground state), and lastly by tellurides (0 – 50 meV/atom above the ground state).[111] When evaluating the feasibility of isolating hypothetical metastable polymorphs, these findings provide insight as to which structures should be attainable from a thermodynamic perspective for different chemistries.

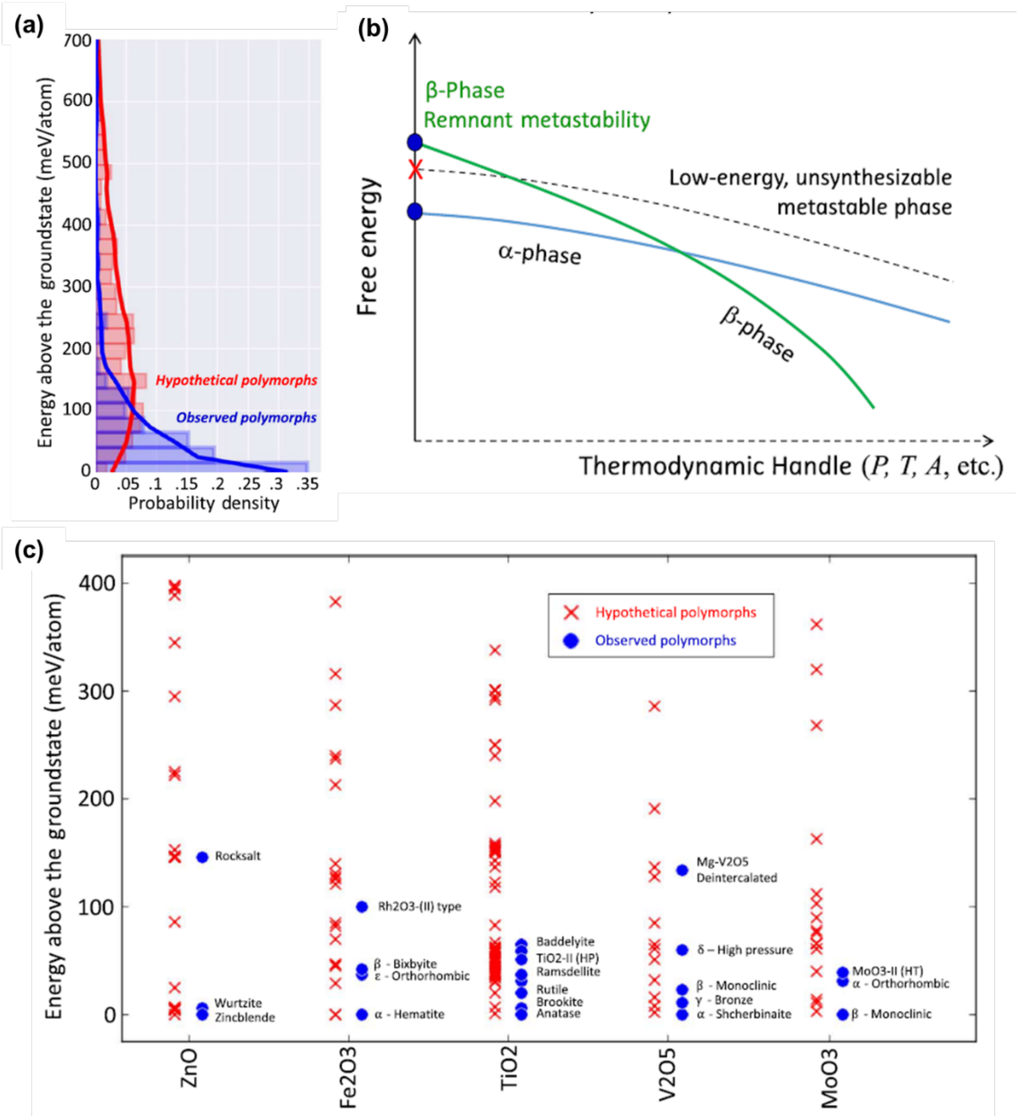

Figure 12. (a) Probability density of metastable binary metal oxide polymorphs *vs* the polymorph energies above the ground state. The blue curve represents the trend for experimentally observed polymorphs, while the red curve represents the trend for hypothetical, unobserved metastable polymorphs. (b) Graph demonstrating the requirement of "remnant stability" for the syntheses of metastable polymorphs. (c) Plot of the calculated energies of experimentally observed polymorphs (blue points) and unobserved polymorphs (red points) for different binary metal oxides. Note that for each material, there exist hypothetical polymorphs that fall energetically between experimentally observed polymorphs, proving that energy above the ground state is not the only factor in determining synthesizability of metastable polymorphs. Reprinted from reference [111]. 2016 © The Authors, some rights reserved; exclusive licensee American Association for the Advancement of Science. Distributed under a Creative Commons Attribution NonCommercial License 4.0 (CC BY-NC).

The stipulation of remnant stability limits the number of possible isolable polymorphs and suggests that by expanding our knowledge of the thermodynamic stabilities of material systems under variable conditions, we can identify which metastable polymorphs should be attainable. While insightful, it is difficult to extend this principle to the nanoscale due to the aforementioned complexity of parameters that influence thermodynamic stabilities of nanomaterials, including surface energy, morphology, defects, surface ligand interactions, size effects, composition, etc. Recently, we proposed a conceptual framework that utilizes thermodynamic bulk phase diagrams to target material systems that may yield novel metastable polymorphs on the nanoscale.[67] This framework was developed after noting emerging patterns in our studies of the mechanisms of formation for metastable wurtzite-like $CuInSe_2$ and $AgInSe_2$ nanocrystals; in both cases, the metastable ternary wurtzite-like phases form as In^{3+} reacts with binary selenide intermediates (Cu_3Se_2 or orthorhombic Ag_2Se, respectively) that possess pseudo-hexagonal Se^{2-} sub-lattices and are metastable at the reaction temperatures (vide supra).[65,67] Kinetically fast topotactic cation exchange reactions preserve the hexagonal structures of the intermediates and generate the metastable hexagonal ternary nanocrystals. While the chalcopyrite phase is the thermodynamically stable polymorph for both $CuInSe_2$ and $AgInSe_2$, producing this phase from Cu_3Se_2 or orthorhombic Ag_2Se is kinetically slow due to the activation energy barrier associated with reorganizing the Se^{2-} sub-lattices of the intermediates from nearly hexagonal frameworks to face-centered cubic frameworks. As depicted in **Figure 13**, these "lattice mismatches" between binary and ternary material systems allow kinetic pathways to prevail over thermodynamic pathways, and lead to the formation of ternary metastable materials.

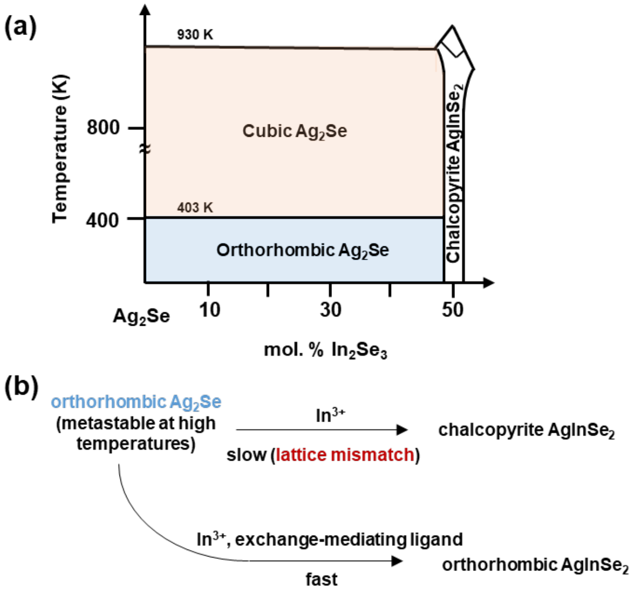

Figure 13. (a) Simplified pseudo-binary Ag_2Se-In_2Se_3 phase diagram. Lattice mismatches between phases are color-coded, where red = body-centered cubic Se^{2-} sub-lattice, blue = pseudo-hexagonal Se^{2-} sub-lattice, and white = face-centered cubic Se^{2-} sub-lattice. (b) Reaction scheme demonstrating how the lattice mismatch between orthorhombic Ag_2Se and chalcopyrite $AgInSe_2$ prevents the thermodynamic pathway from operating, allowing the system to follow the kinetically faster pathway to yield metastable orthorhombic $AgInSe_2$. Adapted with permission from reference [67], copyright 2020, American Chemical Society, and reference [101], copyright 2001, Elsevier.

In seeking to synthesize new metastable polymorphs on the nanoscale, chemists should consult pseudo-binary or ternary phase diagrams to design syntheses that exploit the kinetic advantages afforded by such lattice mismatches. This approach, when combined with DFT calculations that shed light on the relative thermodynamic stabilities of predicted metastable phases, should provide chemists with a method of predictably synthesizing novel metastable polymorphs on the nanoscale. Additionally, although not covered in this review, machine learning tools are becoming more widely used in materials research in general, and promise to further expand our reach into the realm of new metastable nanomaterials syntheses.[112–115]

3. Properties and Applications of Semiconductor Nanocrystals with Metastable Crystal Structures

Interest in metastable materials is driven by their potential to manifest new functional properties. However, in addition to physical properties, the kinetic persistence of metastable materials is an important metric in determining the utility of metastable materials for technological applications. For instance, the metastable halide perovskite-phase of $CsPbI_3$ represents a noteworthy example in which the physical properties of the material are highly desirable for applications in solar cells and LEDs, but its commercial use will be limited by the relatively fast relaxation to the "nonfunctional" thermodynamically stable orthorhombic phase.[93,116,117] For the purposes of this review, discussion of the applications, properties, and persistence of metastable polymorphic nanomaterials will be limited to those discussed in **Section 2**. While these materials have potential applications ranging from infrared emitters for biological imaging,[99,109] to solar cells,[118,119] and non-linear optics,[110] we will highlight work in this section that explicitly demonstrates new functional properties brought about by metastable crystal structures. That said, the field of metastable polymorphic nanomaterials has thus far primarily focused on the syntheses of metastable nanomaterials, and much still remains to be discovered regarding the properties of many of these novel systems.

3.1 Metastable Wurtzite ZnSe Nanocrystals

3.1.1 Optical Properties and Electrochemiluminescence Applications of Wurtzite ZnSe Nanocrystals

Metastable wurtzite zinc selenide nanocrystals exhibit several notably different optical properties compared to the zinc blende polymorph. For example, emission from zinc blende ZnSe nanowires is polarized parallel to the direction of the nanowire, while polarized photoluminescence occurs perpendicular to the *c*-axis of wurtzite ZnSe nanowires.[120] This property makes wurtzite ZnSe useful for single-photon emitters. When excited with light, electron-hole pairs within the wurtzite nanowires form transient dipoles perpendicular to long axis of the nanowire (*c*-axis); such orthogonal dipoles are necessary to achieve the highest possible rates of photon emission, whereas in zinc blende ZnSe, the transient excitonic dipoles form parallel to the direction of the nanowire, which reduces photon extraction efficiencies.[120,121] In addition to photonics, the wurtzite phase may be preferable to the zinc blende phase for electrochemiluminescence applications.[122] Electrochemiluminescence (ECL) is the process whereby species generated at electrode surfaces react to yield electronic excited states that luminesce. ECL is a highly sensitive technique that can be used to detect chemical and biological analytes in solution.[123]

In their studies of ZnSe as a material for ECL applications, Dai et al. found that wurtzite ZnSe nanocrystals possess defective segments that break the translational symmetry of the crystal, as illustrated by aberration-corrected high-angle annular-dark-field (HAADF) images of wurtzite ZnSe nanocrystals in **Figure 14**. Such symmetry-breaking defects induce local charge imbalances within the material, and result in novel optical properties.[122,124] Zinc blende ZnSe nanocrystals also displayed symmetry-breaking defects, although electron holography experiments revealed that the net local charges in defective segments of ZnSe nanocrystals were greater in the wurtzite phase than in the zinc blende phase.[122]

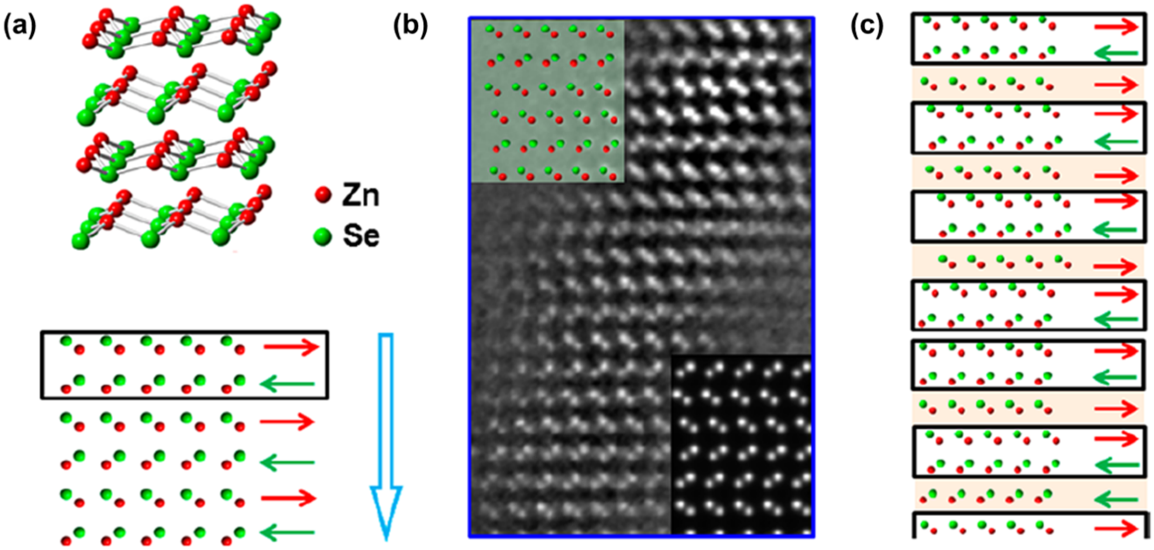

Figure 14. (a) Depiction of the defect-free ABAB stacking in wurtzite ZnSe. The alternating direction of the Zn-Se bond is indicated by red and green arrows. (b) Aberration-corrected high-angle annular-dark-field (HAADF) image of wurtzite ZnSe nanocrystals containing symmetry-breaking defects. In the upper left corner, a structural model is superimposed upon the image. The bottom right corner is a simulated HAADF representation of the experimental data. (c) Model representing the atomic structure found in (b); note that the translational symmetry of the direction of the Zn-Se bond is broken here, as compared to in (a). Adapted with permission from reference [122], copyright 2016, American Chemical Society.

To test the application of these nanocrystals as ECL sensors, electrodes modified with ZnSe were fabricated and subject to reductive potentials in the presence of aqueous $K_2S_2O_8$ as a co-reactant. Under these conditions, $S_2O_8^{2-}$ reduces to form equivalents of $SO_4^{\bullet-}$, a powerful oxidant. It is speculated the symmetry-breaking defects result in electron injection into the conduction band of ZnSe in negatively charged defect regions of the ZnSe nanocrystals. These negatively charged domains are oxidized by $SO_4^{\bullet-}$, producing SO_4^{2-} and a charge-neutral excited state of ZnSe that can then undergo radiative relaxation. This proposed ECL mechanism is depicted in **Figure 15a**.

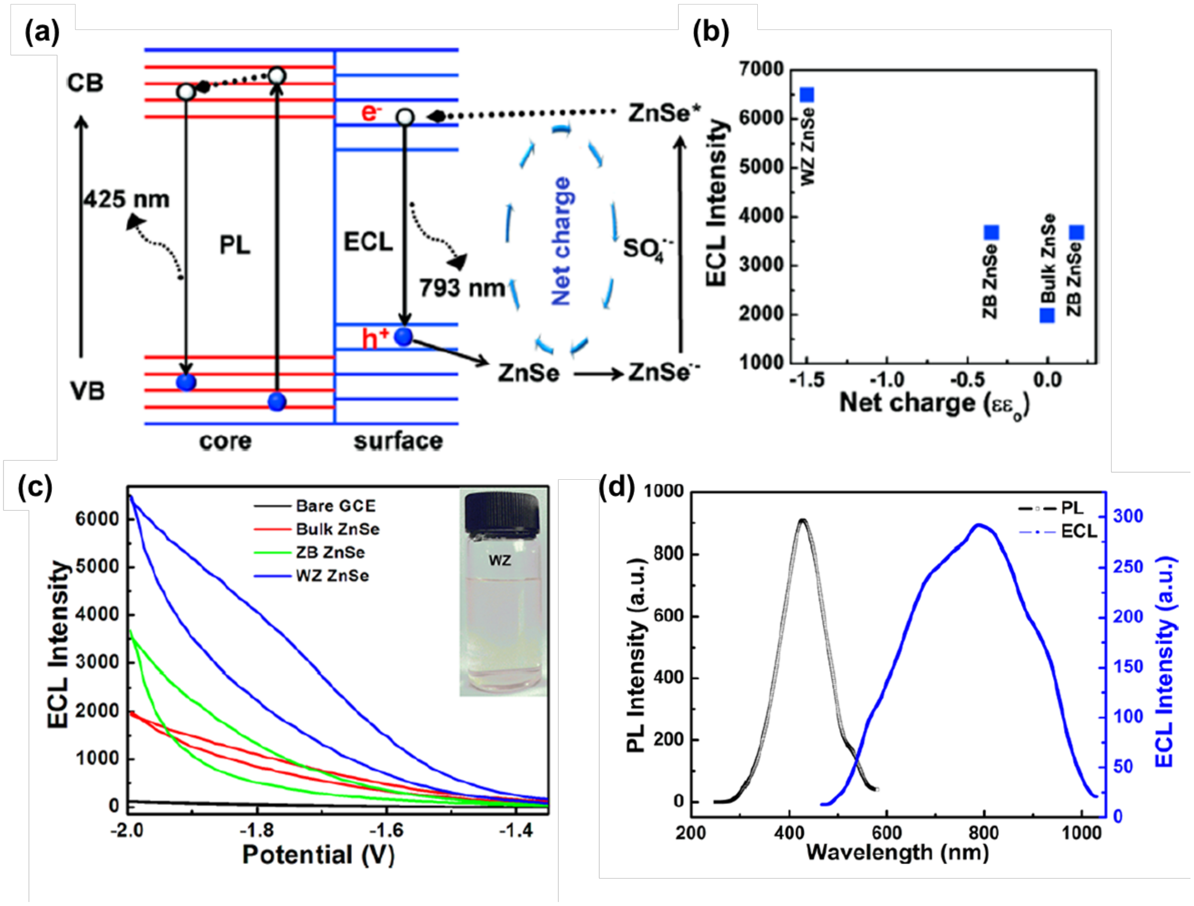

Figure 15. (a) ECL mechanism that elucidates interactions between $SO_4^{\bullet -}$ and negatively charged ZnSe. (b) Plot of ECL signal intensity as a function of the net charge of defect regions in different forms of ZnSe, as measured by electron holography. Note that wurtzite ZnSe has the highest charge and also the greatest ECL intensity. (c) Potential-dependent ECL intensity for wurtzite ZnSe, zinc blende ZnSe, bulk ZnSe, and the bare glassy-carbon electrode. (d) The ECL signal (blue curve) is significantly red-shifted from the intrinsic photoluminescence (black curve) of wurtzite ZnSe nanocrystals, suggesting ECL originates from an intra-gap surface trap state. Adapted with permission from reference [122], copyright 2016, American Chemical Society.

Importantly, the greater excess of charge in wurtzite ZnSe defect segments was found to enhance probability of electron-hole recombination in wurtzite ZnSe, translating into more intense electrochemiluminescence from these nanocrystals as compared to zinc blende ZnSe nanocrystals or bulk zinc blende ZnSe (**Figure 15b,c**). ECL is notably red-shifted from the intrinsic photoluminescence of the ZnSe nanocrystals, suggesting that ECL originates from relaxation of electrons in intra-gap surface trap states (**Figure 15d**).[122] These results show that the defect chemistry can differ between polymorphs, and that defects play a role in influencing the properties of the metastable nanomaterials.

3.2 Metastable Wurtzite-Like $CuInSe_2$ Nanocrystals

3.2.1 Electronic Structure of Wurtzite-Like $CuInSe_2$

As mentioned in **2.2.1**, $CuInSe_2$ is an excellent candidate for application in thin-film photovoltaics due to its relatively low toxicity and direct band gap of ~1.0 eV.[125] Lau et al. sought to explore the properties of the metastable wurtzite-like phase of $CuInSe_2$ through a first-principles DFT study.[126] The wurtzite-like phase in this study was characterized by an ordering of the Cu^{+} and In^{3+} sites within a hexagonally close-packed framework of Se^{2-}; such ordering has been experimentally verified for wurtzite-like $CuInSe_2$ nanocrystals.[79] The valence band maximum (VBM) of the chalcopyrite $CuInSe_2$ has antibonding character arising from interactions between Cu *d*-states and Se *p*-states.[127] The Cu *d*-electrons are relatively localized and contribute little to the density of states near the Fermi energy, as shown in **Figure 16a**. In contrast, greater hybridization of Cu *d*-states with In and Se *p*-states reduces the localization of Cu *d*-electrons in wurtzite-like $CuInSe_2$ and results greater density of states near the Fermi energy (**Figure 16a**), which should theoretically enhance electronic excitation and transport in $CuInSe_2$.[126]

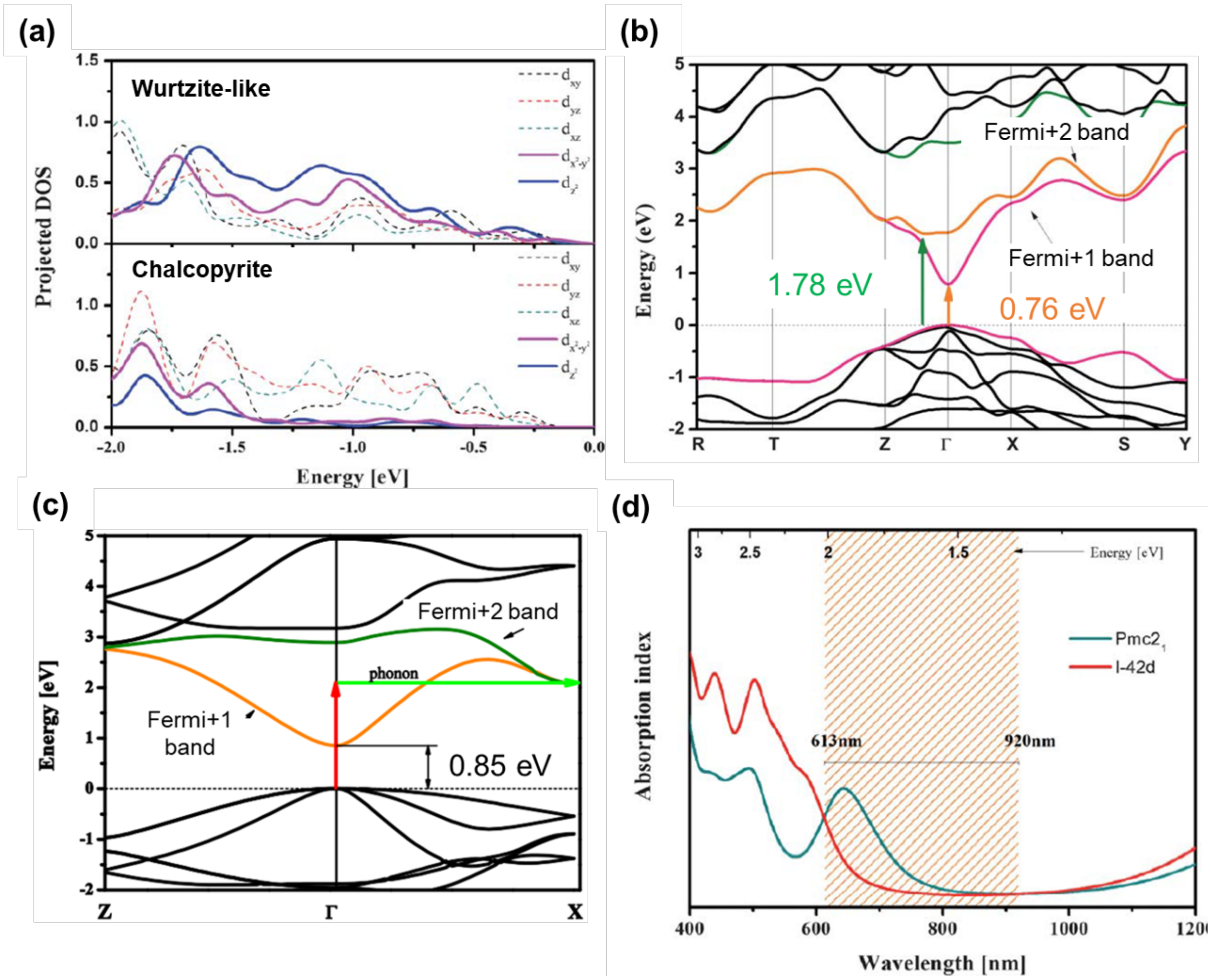

Figure 16. (a) Calculated density of states for Cu *d*-states for wurtzite-like (top) and chalcopyrite (bottom) $CuInSe_2$. The Fermi energy is set to zero. (b) Calculated band structure for wurtzite-like $CuInSe_2$. (c) Calculated band structure for chalcopyrite $CuInSe_2$. (d) Simulated electronic absorption profiles for wurtzite-like and chalcopyrite $CuInSe_2$; note that the wurtzite-like phase is expected to display comparable or superior absorption to the chalcopyrite phase from 920 – 613 nm (1.35 – 2.0 eV) of the electromagnetic spectrum. Adapted with permission from reference [126], copyright 2012, Royal Society of Chemistry.

Moreover, the calculated electronic band structure of the wurtzite-like phase suggests that this phase may be a more efficient absorber of the solar spectrum than the chalcopyrite phase. **Figure 16b,c** indicates that, while both polymorphs have narrow, direct band gaps, light absorption in the wurtzite-like phase should be enhanced compared to the chalcopyrite phase due to a near-direct transition from the VBM to the minimum of the Fermi+1 conduction band. In the chalcopyrite phase, this excitation is an indirect, phonon-assisted transition, making it less probable than in the wurtzite-like phase. **Figure 16d** illustrates that the calculated electronic absorption for wurtzite-like $CuInSe_2$ is greater than that of the chalcopyrite phase through the range of the electromagnetic spectrum most relevant for solar cells.[126] In addition to the favorable electronic band structure of wurtzite-like $CuInSe_2$, wurtzite and wurtzite-like phases are often more compositionally flexible than other polymorphs of I-III-VI_2 semiconductors (see **Figures 5, 9**), which opens opportunities for fine tuning of the composition-dependent band gaps of these materials.[128] Such strategies have been successfully employed for band gap engineering in similar material systems. Indeed, by synthetically tuning the S:Se ratio in wurtzite-like $CuZnSn(S_{1-x}Se_x)_4$ nanocrystals, the band gap can be linearly tuned from 1.0 to 1.5 eV, which is a wider range than afforded through the same compositional tuning within the thermodynamically preferred kesterite polymorph of $CuZnSn(S_{1-x}Se_x)_4$.[58,59]

3.2.2 Persistence of Wurtzite-like $CuInSe_2$ Nanocrystals

Lau et al. calculated that the wurtzite-like phase of $CuInSe_2$ is metastable with respect to the chalcopyrite polymorph by a mere 5-9 meV/atom (at 0 K), and that there exists a large activation energy barrier to convert between these two phases.[126] Indeed, we experimentally verified the temporal and thermal stability of the wurtzite-like phase in $CuInSe_2$ nanocrystals.[65] Post-synthetically heating wurtzite-like $CuInSe_2$ nanocrystals to 300 °C in solution failed to induce a phase transition to the thermodynamically stable chalcopyrite phase. Similar results were found when the nanocrystals in powder form were exposed to multiple heating-cooling cycles to 300 °C. Only when the nanocrystals were heated past the temperature (420 °C) at which the oleylamine ligands volatilize from surface of the nanocrystals did we observe a phase transition to the chalcopyrite phase. This thermal stability is remarkable for a metastable nanocrystalline polymorph, especially considering that the temperature of solid-solid phase transitions are often substantially reduced on the nanoscale.[129–131] These experiments, and the fact that we observed wurtzite-like phase $CuInSe_2$ nanocrystals to show no sign of relaxation to the chalcopyrite phase after one year,[65] support calculations that predict the wurtzite-like polymorph to be a highly persistent, deep local minimum within the energetic landscape of polymorphic $CuInSe_2$. This profound kinetic trapping of the metastable phase may be common to many material systems capable of crystallizing with wurtzite-like structure types; we experimentally showed that a similar wurtzite-like phase of $AgInSe_2$ nanocrystals displayed comparable temporal and thermal persistence to that of wurtzite-like $CuInSe_2$,[65] and Ryan et al. found the wurtzite-like phase of $CuZnSnS_4$ nanocrystals to be persistent up to ~380 °C.[132]

3.3 Metastable Ag_2Se Nanocrystals

3.3.1 Superionic Conducting Cubic Ag_2Se Nanocrystals for Catalyzed Nanowire Growth

As discussed in **2.3.1**, Ag_2Se has two polymorphs in bulk, namely the low- and high-temperature orthorhombic and cubic phases, respectively, and an additional metastable tetragonal polymorph that only forms on the nanoscale. Physicochemical property differences often exist between polymorphic materials. For example, the orthorhombic-to-cubic phase transition in Ag_2Se is accompanied by changes to the electronic structure of Ag_2Se. At low temperatures, orthorhombic Ag_2Se is a low-band gap semiconductor. Upon transitioning to cubic Ag_2Se, the material becomes both electronically metallic and a superionic conductor in which mobile Ag^+ ions are capable of collective motion within the body-centered cubic framework of Se^{2-} anions.[133–137]

While an exhaustive assessment of all applications of Ag_2Se is beyond the scope of this review, the unique properties of different polymorphs of Ag_2Se, and the ability to control phase transitions between polymorphs on the nanoscale, makes this material system attractive for thermoelectrics,[135] electrical switches and digital memory storage,[85,138–140] infrared optoelectronic devices,[141] and catalysts for metal chalcogenide nanowire synthesis.[92] The existence of the high-temperature cubic phase and the metastable low-temperature tetragonal phase gives rise to two types of polymorphic metastability at low temperatures, where Ag_2Se can exist in either one of these phases and still be metastable with respect to orthorhombic Ag_2Se. Presented herein are two examples in which metastable cubic and tetragonal Ag_2Se have been exploited for their characteristic properties to introduce new functionalities in nanocrystal syntheses and optoelectronics, respectively.

Thermodynamically, the cubic phase of Ag_2Se is stable above $T > 135$ °C.[86–88] However, this superionic conducting phase can be kinetically trapped at lower temperatures, and has even been observed at room temperature.[138] Yang et al. demonstrated that cubic Ag_2Se can be used to catalyze the low-temperature growth of ZnSe nanowires, enabling nanowire synthesis at temperatures as low as 100 °C, a lower temperature than any previously reported temperatures for the syntheses of crystalline ZnSe nanowires.[92] In their syntheses, nearly equimolar amounts of the zinc and selenium precursors were dissolved and then heated in the presence of a small amount of $AgNO_3$ (roughly 2% of the equivalents of zinc) to produce the Ag_2Se-catalyzed ZnSe nanowires.

Here, the cubic phase plays a pivotal role in the proposed "solution-solid-solid" mechanism of catalyzed nanowire growth: First, the extreme mobility of Ag^+ and the prevalence of vacancies in cubic Ag_2Se favor incorporation of other cations, like Zn^{2+}, into the nanocrystals, leading to an intermediate Ag-Zn-Se solid solution. However, since the solubility of ZnSe in Ag_2Se at low temperatures is small, the solid solution quickly becomes supersaturated with Zn^{2+}, facilitating a phase-segregating process in which ZnSe precipitates from Ag_2Se, effectively regenerating the catalyst. Once a Ag_2Se-ZnSe solid-solid interface is established, diffusion of cations (both Ag^+ into ZnSe and Zn^{2+} into Ag_2Se) across the interface encourages further growth of ZnSe at the interface as more Zn^{2+} is incorporated from solution into vacancies created as a consequence of cation migration.

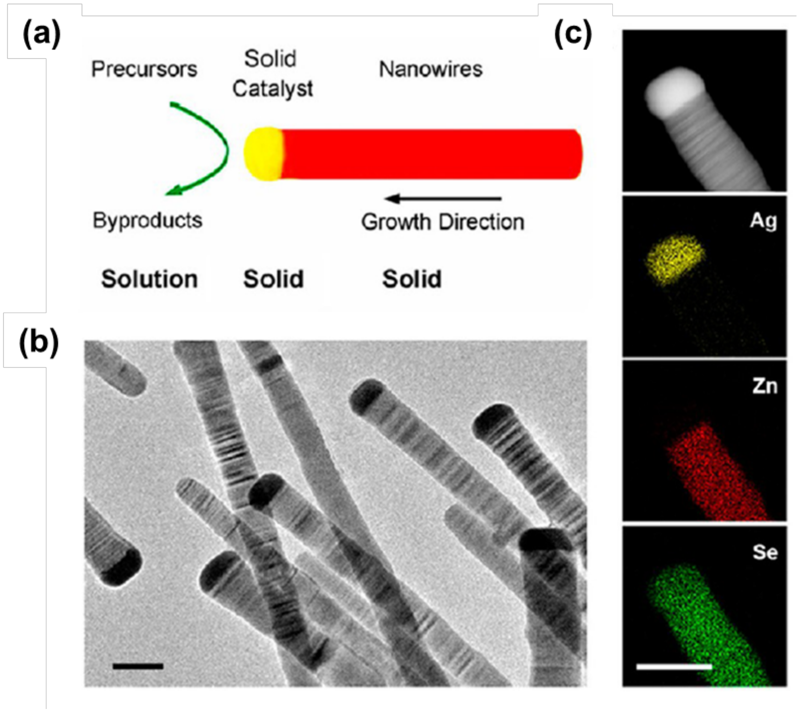

Figure 17. (a) Scheme illustrating the proposed solution-solid-solid mechanism of cubic Ag_2Se-catalyzed ZnSe nanowire growth. (b) TEM micrograph of ZnSe nanowires grown via Ag_2Se catalysis. Note that the nanowires are capped with Ag_2Se tips. (c) Scanning TEM micrograph and energy-

dispersive spectroscopy elemental mapping of ZnSe nanowires capped with the Ag_2Se tip. Adapted with permission from reference [92], copyright 2013, American Chemical Society.

Yang et al. hypothesize that it is this migration of cations through the solid-solid interface that drives anisotropic growth of ZnSe. The Ag_2Se-catalyzed mechanism of ZnSe nanowire growth is depicted in **Figure 17a**, along with TEM micrographs and energy-dispersive spectroscopy elemental mapping of the nanocrystals in **Figure 17b,c**. They found this method of catalysis with cubic Ag_2Se could be extended to the low-temperature synthesis of crystalline CdSe nanowires, and that superionic Ag_2S and Cu_2S nanocrystals are capable of catalyzing nanowire growth as well.[92]

3.3.2 Optoelectronic Properties of Tetragonal Ag_2Se Nanocrystals

In contrast to the metallic, superionic conducting cubic phase, the metastable tetragonal phase of Ag_2Se is a narrow band gap semiconductor. However, due to the fact it only arises on the nanoscale, relatively little is known about the tetragonal phase of Ag_2Se in comparison to the orthorhombic or cubic phases. In the first detailed study of the optical properties of tetragonal Ag_2Se nanocrystals, Norris et al. showed that this material shows promise for use as emitters or detectors of the mid-infrared region of the electromagnetic spectrum.[141] Importantly, Ag_2Se is less toxic than other materials, such as HgTe or HgCdTe, that are employed in mid-infrared optoelectronics.[142]

By synthesizing tetragonal Ag_2Se nanocrystals of different sizes (2.7 – 10.4 nm in diameter), Norris et al. were able to systematically tune the optical band gap of the material. Indeed, they calculated the Bohr exciton radius of this phase to be roughly 2.9 nm, indicating that any nanocrystals under 5.8 nm in diameter should exhibit strong quantum confinement, as shown in **Figure 18c**. While such confinement-induced band gap tunability is ubiquitous in nanocrystal chemistry, tetragonal Ag_2Se nanocrystals afford the unique feature of tunability of absorption in the mid-infrared, exhibiting some of the longest wavelength absorption peaks reported for colloidal nanocrystals, up to 6.5 μm (**Figure 18a, b**).[141]

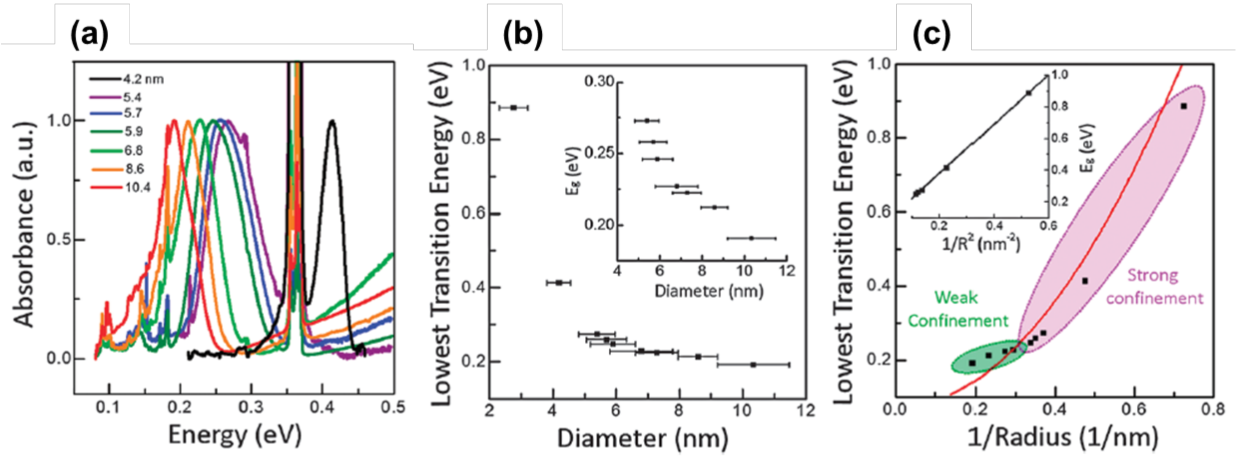

Figure 18. (a) Mid-infrared absorption spectra for tetragonal Ag_2Se nanocrystals of different sizes. The large peak at 0.35 eV corresponds to a solvent absorption peak. (b) Plot of the lowest transition energies for tetragonal Ag_2Se nanocrystals as a function of nanocrystal diameter. (c) Lowest transition energies vs 1/nanocrystal radius. The red curve represents the predicted lowest transition energies as a function of 1/radius as calculated through effective mass theory. This relationship is linear when plotted lowest transition energies versus $1/\text{radius}^2$ (inset). Adapted with permission from reference [141], copyright 2012, Royal Society of Chemistry.

Within the strong confinement regime, there exists a linear relationship between the lowest energy transition of the nanocrystals and 1/nanocrystal radius^2, as pictured in the inset of **Figure 18c**. The effective bulk band gap of tetragonal Ag_2Se is calculated by solving for the y-intercept of the line of best fit of the transition energy vs 1/radius^2, where the y-intercept represents a crystal with an infinite radius. This treatment produces a value of 0.064 eV for the bulk band gap of tetragonal Ag_2Se. Although bulk tetragonal Ag_2Se has never been observed, the minimum experimental band gap observed is roughly 0.07 eV, which fits well with the results of this calculation.[143] Notably, this band gap is less than that of the stable semiconducting orthorhombic phase of Ag_2Se, which has a bulk band gap of 0.15 – 0.18 eV, suggesting that the tetragonal polymorph extends functionality of this material system deeper into the infrared region of the electromagnetic spectrum.[141] Finally, Norris et al. also demonstrated that these tetragonal Ag_2Se nanocrystals fluoresce in the infrared, making them useful for applications as mid-infrared optoelectronic detectors and emitters.[141]

3.3.3 Core-Shell Effects on the High-Temperature Stability of Tetragonal Ag_2Se Nanocrystals

The effects of surface ligands on the temporal and thermal persistence of the metastable tetragonal phase of Ag_2Se has been discussed in **2.3.1**, underscoring that this phase, under certain conditions, can last for a week or longer and can undergo a phase transition to the high-temperature cubic phase of Ag_2Se around ~100 °C. Relevant to the application of Ag_2Se as a material for phase-dependent electrical switching, Norris et al. found that the temperature of the tetragonal-to-cubic phase transition can be increased significantly by installing a shell around tetragonal Ag_2Se nanocrystal cores.[85] In fact, if there is a significant mismatch in lattice parameters between the core and shell materials, the shell can induce pressures on the order of a few gigapascals on the core.[144] In the case of tetragonal Ag_2Se, it was found that the phase transition temperature could be controlled by depositing shells with a lesser lattice mismatch (ZnS, 8.5%) or a greater lattice mismatch (CdS, 17%), as well as by controlling the number of layers of deposited core material. Intriguingly, a 50 °C increase was observed for the tetragonal-to-cubic phase transition when depositing a shell of CdS around the Ag_2Se cores. Similarly, by growing variable thickness shells of ZnS around tetragonal Ag_2Se nanocrystals, the phase transition temperature could be tuned by 30-65 °C.[85] Since cubic Ag_2Se is a metallic superionic conductor, it is useful for electrical switching applications to have such fine control over the temperature at which this phase transition occurs.

4. Conclusions

The direct syntheses of metastable polymorphic nanocrystals are developing from a science reliant on empirical findings to a field equipped with synthetic strategies that allow desired polymorphs to be targeted. In this review, the highlighted methodologies for polymorphic control on the nanoscale included modulation of reaction conditions (temperature, time, concentration, etc.), kinetic control via prudent selection of molecular precursors, ligand effects, and surface chemistry considerations. While these methodologies show broad utility in preparing metastable nanomaterials, they are by no means the only methods of obtaining nanocrystals with metastable crystal structures. Other methods not discussed here, such as those that exploit the hysteresis of pressure-induced phase transitions, have also led to isolation of persistent metastable polymorphs.[145]

Recent data mining research of thousands of inorganic compounds suggests that, in order to be isolable, metastable polymorphs must be thermodynamically favored under some set of conditions, and that their persistence away from thermodynamic equilibrium is evidence of “remnant” thermodynamic stability.[111] This concept is useful in that it places limits on the number of possible metastable polymorphs for a material, reducing the otherwise potentially infinite metastable phase space to a more tractable, albeit, still vast, thermodynamically defined phase space. In this vein, understanding polymorphic metastability from the perspective of thermodynamics compels us to gain a more quantitative knowledge of thermodynamic phase relations on the nanoscale, and how those relations depend on variables such as temperature, surface energy, ligands, composition, etc. If this can be achieved, new metastable nanomaterials might be predictably synthesized by manipulating thermodynamic reaction parameters to target desired polymorphs. However, obtaining quantitative thermodynamic information across multivariate phase spaces on the nanoscale is a Herculean task, due to the myriad variables and complexities of nanoscale material systems. Therefore, the continued development of kinetic frameworks and other methods towards the rational syntheses of metastable polymorphs will likely remain the most practical for discovering new metastable materials. Although not covered in this review, chemists continue to push the boundaries of cation exchange as a highly fruitful method of obtaining new polymorphs. In addition, outlined in this review are examples that demonstrate how bulk thermodynamic phase diagrams can be used to predict the kinetic isolation of metastable polymorphs on the nanoscale. In the near future, machine learning tools promise use in the design of syntheses for metastable nanomaterials.

Metastable polymorphs of semiconductor nanocrystals often manifest distinct physical, chemical, and optoelectronic properties from their thermodynamic congeners. Continued exploration into the syntheses and properties of metastable phase spaces is needed and should be motivated by their potential to afford functional materials for photonics, optical sensing and imaging, solar cells, LEDs, thermoelectrics, and other applications. The selected material case studies in this review highlight explicit examples in which metastable polymorphs yield new functional properties that open doors to enhanced device performances or completely novel applications that could not be achieved without access to these metastable phases. The study of the properties and technological applications of metastable polymorphic nanomaterials is a broad field in its own right and deserves a more in-depth review than is possible here.

Acknowledgements

This work was supported by the U.S. Department of Energy, Office of Science, Basic Energy Sciences, under award DE-FG02-11ER46826.

Notes

The authors declare no competing financial interests.
*Email: brutchey@usc.edu

References

[1] F. P. Bundy, W. A. Bassett, M. S. Weathers, R. J. Hemley, H. U. Mao, A. F. Goncharov, *Carbon* **1996**, *34*, 141–153.
[2] B. V. Derjaguin, D. B. Fedoseev, *Prog. Surf. Sci.* **1994**, *45*, 57–64.
[3] J. C. Angus, Y. Wang, M. Sunkara, *Annu. Rev. Mater. Sci.* **1991**, *21*, 221–248.
[4] J. C. Angus, *Diam. Relat. Mater.* **2014**, *49*, 77–86.
[5] F. P. Bundy, H. T. Hall, H. M. Strong, R. H. Wentorfjun, *Nature* **1955**, *176*, 51–55.
[6] H. M. Lu, Q. Jiang, *J. Phys. Chem. B* **2004**, *108*, 5617–5619.
[7] H. Zhang, B. Gilbert, F. Huang, J. F. Banfield, *Nature* **2003**, *424*, 1025–1029.
[8] P. D. Cozzoli, L. Manna, M. L. Curri, S. Kudera, C. Giannini, M. Striccoli, A. Agostiano, *Chem. Mater.* **2005**, *17*, 1296–1306.
[9] A. Navrotsky, *MRS Bull.* **2016**, *41*, 139–145.
[10] J. M. McHale, A. Auroux, A. J. Perrotta, A. Navrotsky, *Science* **1997**, *277*, 788–791.
[11] A. S. Barnard, L. A. Curtiss, *Nano Lett.* **2005**, *5*, 1261–1266.
[12] D. H. Son, S. M. Hughes, Y. Yin, A. P. Alivisatos, *Science* **2004**, *306*, 1009–1012

[13] J. Wang, W. Fan, J. Yang, Z. Da, X. Yang, K. Chen, H. Yu, X. Cheng, *Chem. Mater.* **2014**, *26*, 5647–5653.
[14] Y. Saito, M. Sato, M. Shiojiri, *Thin Solid Films* **1981**, *79*, 257–266.
[15] J. R. Günter, P. Keusch, *Ultramicroscopy* **1993**, *49*, 293–307.
[16] T. Okabe, K. Ura, *J. Appl. Crystallogr.* **1994**, *27*, 140–145.
[17] E. A. Hernández-Pagán, E. H. Robinson, A. D. La Croix, J. E. Macdonald, *Chem. Mater.* **2019**, *31*, 4619–4624.
[18] M. T. Ng, C. B. Boothroyd, J. J. Vittal, *J. Am. Chem. Soc.* **2006**, *128*, 7118–7119.
[19] R. B. Soriano, I. U. Arachchige, C. D. Malliakas, J. Wu, M. G. Kanatzidis, *J. Am. Chem. Soc.* **2013**, *135*, 768–774.
[20] M. E. Norako, R. L. Brutchey, *Chem. Mater.* **2010**, *22*, 1613–1615.
[21] M. E. Norako, M. J. Greaney, R. L. Brutchey, *J. Am. Chem. Soc.* **2012**, *134*, 23–26.
[22] X. Lu, Z. Zhuang, Q. Peng, Y. Li, *Chem. Commun.* **2011**, *47*, 3141–3143.
[23] J.-J. Wang, J.-S. Hu, Y.-G. Guo, L.-J. Wan, *NPG Asia Mater.* **2012**, *4*, e2–e2.
[24] A. Parija, G. R. Waetzig, J. L. Andrews, S. Banerjee, *J. Phys. Chem. C* **2018**, *122*, 25709–25728.
[25] A. J. Martinolich, J. R. Neilson, *Chem. Mater.* **2017**, *29*, 479–489.
[26] A. J. Martinolich, J. A. Kurzman, J. R. Neilson, *J. Am. Chem. Soc.* **2015**, *137*, 3827-3833.
[27] V. Lesnyak, R. Brescia, G. C. Messina, L. Manna, *J. Am. Chem. Soc.* **2015**, *137*, 9315–9323.
[28] J. B. Rivest, P. K. Jain, *Chem. Soc. Rev.* **2012**, *42*, 89–96.
[29] L. D. Trizio, L. Manna, *Chem. Rev.* **2016**, *116*, 10852–10887.
[30] S. O. M. Hinterding, A. C. Berends, M. Kurttepeli, M.-E. Moret, J. D. Meeldijk, S. Bals, W. van der Stam, C. de Mello Donega, *ACS Nano* **2019**, *13*, 12880–12893.
[31] A. E. Powell, J. M. Hodges, R. E. Schaak, *J. Am. Chem. Soc.* **2016**, *138*, 471–474.
[32] H. Li, M. Zanella, A. Genovese, M. Povia, A. Falqui, C. Giannini, L. Manna, *Nano Lett.* **2011**, *11*, 4964–4970.
[33] J. M. Hodges, K. Kletetschka, J. L. Fenton, C. G. Read, R. E. Schaak, *Angew. Chem. Int. Ed.* **2015**, *54*, 8669–8672.
[34] B. J. Beberwyck, Y. Surendranath, A. P. Alivisatos, *J. Phys. Chem. C* **2013**, *117*, 19759–19770.
[35] G. Cho, Y. Park, Y.-K. Hong, D.-H. Ha, *Nano Converg.* **2019**, *6*, 17.
[36] Y. Yin, A. P. Alivisatos, *Nature* **2005**, *437*, 664–670.
[37] J. Park, J. Joo, S. G. Kwon, Y. Jang, T. Hyeon, *Angew. Chem. Int. Ed.* **2007**, *46*, 4630–4660.
[38] G. Barim, S. R. Smock, P. D. Antunez, D. Glaser, R. L. Brutchey, *Nanoscale* **2018**, *10*, 16298–16306.
[39] L. Mora-Tamez, G. Barim, C. Downes, E. M. Williamson, S. E. Habas, R. L. Brutchey, *Chem. Mater.* **2019**, *31*, 1552–1560.
[40] B. Cao, L. A. Adutwum, A. O. Oliynyk, E. J. Luber, B. C. Olsen, A. Mar, J. M. Buriak, *ACS Nano* **2018**, *12*, 7434–7444.
[41] L. S. Li, N. Pradhan, Y. Wang, X. Peng, *Nano Lett.* **2004**, *4*, 2261–2264.
[42] H. K. Sadekar, A. V. Ghule, R. Sharma, *Compos. Part B Eng.* **2013**, *44*, 553–557.
[43] P. Reiss, *New J. Chem.* **2007**, *31*, 1843–1852.
[44] C.-Y. Yeh, Z. W. Lu, S. Froyen, A. Zunger, *Phys. Rev. B* **1992**, *46*, 10086–10097.
[45] H. Okada, T. Kawanaka, S. Ohmoto, *J. Cryst. Growth* **1996**, *165*, 31–36.
[46] P. Masri, *Surf. Sci. Rep.* **2002**, *48*, 1–51.
[47] T. Sugimoto, *Monodispersed Particles*, Elsevier Science B.V., Amsterdam, Netherlands, **2001**.
[48] S. Li, G. W. Yang, *J. Phys. Chem. C* **2010**, *114*, 15054–15060.
[49] J. Huang, M. V. Kovalenko, D. V. Talapin, *J. Am. Chem. Soc.* **2010**, *132*, 15866–15868.
[50] M. Green, *Semiconductor Quantum Dots: Organometallic and Inorganic Synthesis*, Royal Society of Chemistry, Cambridge, UK, **2014**.
[51] J. Wang, P. Liu, C. C. Seaton, K. M. Ryan, *J. Am. Chem. Soc.* **2014**, *136*, 7954–7960.
[52] J.-J. Wang, K. M. Ryan, *CrystEngComm* **2016**, *18*, 3161–3169.

[53] J. Wang, A. Singh, P. Liu, S. Singh, C. Coughlan, Y. Guo, K. M. Ryan, *J. Am. Chem. Soc.* **2013**, *135*, 7835–7838.
[54] Materials Science International Team, in *Non-Ferr. Met. Syst. Part 1*, Springer-Verlag, Berlin/Heidelberg, Germany, **2006**.
[55] S. Schlecht, M. Budde, L. Kienle, *Inorg. Chem.* **2002**, *41*, 6001–6005.
[56] R. L. Brutchey, *Acc. Chem. Res.* **2015**, *48*, 2918–2926.
[57] M. E. Norako, M. A. Franzman, R. L. Brutchey, *Chem. Mater.* **2009**, *21*, 4299–4304.
[58] A. Singh, S. Singh, S. Levcenko, T. Unold, F. Laffir, K. M. Ryan, *Angew. Chem. Int. Ed.* **2013**, *52*, 9120–9124.
[59] F.-J. Fan, L. Wu, M. Gong, G. Liu, Y.-X. Wang, S.-H. Yu, S. Chen, L.-W. Wang, X.-G. Gong, *ACS Nano* **2013**, *7*, 1454–1463.
[60] M. P. Hendricks, M. P. Campos, G. T. Cleveland, I. J.-L. Plante, J. S. Owen, *Science* **2015**, *348*, 1226–1230.
[61] M. J. Thompson, T. P. A. Ruberu, K. J. Blakeney, K. V. Torres, P. S. Dilsaver, J. Vela, *J. Phys. Chem. Lett.* **2013**, *4*, 3918–3923.
[62] R. García-Rodríguez, M. P. Hendricks, B. M. Cossairt, H. Liu, J. S. Owen, *Chem. Mater.* **2013**, *25*, 1233–1249.
[63] Y. Guo, S. R. Alvarado, J. D. Barclay, J. Vela, *ACS Nano* **2013**, *7*, 3616–3626.
[64] J. M. Rhodes, C. A. Jones, L. B. Thal, J. E. Macdonald, *Chem. Mater.* **2017**, *29*, 8521–8530.
[65] B. A. Tappan, G. Barim, J. C. Kwok, R. L. Brutchey, *Chem. Mater.* **2018**, *30*, 5704–5713.
[66] J.-J. Wang, Y.-Q. Wang, F.-F. Cao, Y.-G. Guo, L.-J. Wan, *J. Am. Chem. Soc.* **2010**, *132*, 12218–12221.
[67] B. A. Tappan, M. K. Horton, R. L. Brutchey, *Chem. Mater.* **2020**, *32*, 2935–2945.
[68] S. Li, X. Tang, Z. Zang, Y. Yao, Z. Yao, H. Zhong, B. Chen, *Chin. J. Catal.* **2018**, *39*, 590–605.
[69] M. Sandroni, K. D. Wegner, D. Aldakov, P. Reiss, *ACS Energy Lett.* **2017**, *2*, 1076–1088.
[70] T. Havlik, *Hydrometallurgy: Principles and Applications*, Cambridge International Science Publishing Ltd., Cambridge, England, **2014**.
[71] K. S. Knight, *Mater. Res. Bull.* **1992**, *27*, 161–167.
[72] M. L. Fearheiley, *Sol. Cells* **1986**, *16*, 91–100.
[73] J. S. Park, Z. Dong, S. Kim, J. H. Perepezko, *J. Appl. Phys.* **2000**, *87*, 3683–3690.
[74] S.-H. Wei, L. G. Ferreira, A. Zunger, *Phys. Rev. B* **1992**, *45*, 2533–2536.
[75] J. J. M. Binsma, L. J. Giling, J. Bloem, *J. Cryst. Growth* **1980**, *50*, 429–436.
[76] I. V. Bodnar, I. T. Bodnar, A. A. Vaipolin, *Cryst. Res. Technol.* **1984**, *19*, 1553–1557.
[77] D. Pan, L. An, Z. Sun, W. Hou, Y. Yang, Z. Yang, Y. Lu, *J. Am. Chem. Soc.* **2008**, *130*, 5620–5621.
[78] Y. Qi, Q. Liu, K. Tang, Z. Liang, Z. Ren, X. Liu, *J. Phys. Chem. C* **2009**, *113*, 3939–3944.
[79] V. Sousa, B. F. Gonçalves, M. Franco, Y. Ziouani, N. González-Ballesteros, M. Fátima Cerqueira, V. Yannello, K. Kovnir, O. I. Lebedev, Y. V. Kolen'ko, *Chem. Mater.* **2019**, *31*, 260–267.
[80] X. Shen, E. A. Hernández-Pagan, W. Zhou, Y. S. Puzyrev, J.-C. Idrobo, J. E. Macdonald, S. J. Pennycook, S. T. Pantelides, *Nat. Commun.* **2014**, *5*, 5431.
[81] V. M. Glazov, A. S. Pashinkin, V. A. Fedorov, *Inorg. Mater.* **2000**, *36*, 641–652.
[82] M. M. Parish, P. B. Littlewood, *Nature* **2003**, *426*, 162–165.
[83] M. Ferhat, J. Nagao, *J. Appl. Phys.* **2000**, *88*, 813–816.
[84] P. Boolchand, W. J. Bresser, *Nature* **2001**, *410*, 1070–1073.
[85] A. Sahu, D. Braga, O. Waser, M. S. Kang, D. Deng, D. J. Norris, *Nano Lett.* **2014**, *14*, 115–121.
[86] G. A. Wiegers, *Am. Mineral.* **1971**, *56*, 1882–1888.
[87] I. Karakaya, W. T. Thompson, *Bull. Alloy Phase Diagr.* **1990**, *11*, 266.
[88] V. Buschmann, G. Van Tendeloo, P. Monnoyer, J. B. Nagy, *Langmuir* **1998**, *14*, 1528–1531.
[89] A. Sahu, L. Qi, M. S. Kang, D. Deng, D. J. Norris, *J. Am. Chem. Soc.* **2011**, *133*, 6509–6512.
[90] H. Lu, R. L. Brutchey, *Chem. Mater.* **2017**, *29*, 1396–1403.
[91] J. L. Wang, H. Feng, W. L. Fan, *Advanced Materials Research* **2014**, *850-851*, 128–131.

[92] J. Wang, K. Chen, M. Gong, B. Xu, Q. Yang, *Nano Lett.* **2013**, *13*, 3996–4000.

[93] Y. Fu, T. Wu, J. Wang, J. Zhai, M. J. Shearer, Y. Zhao, R. J. Hamers, E. Kan, K. Deng, X.-Y. Zhu, S. Jin, *Nano Lett.* **2017**, *17*, 4405–4414.

[94] D. Deng, L. Qu, Y. Gu, *J. Mater. Chem. C* **2014**, *2*, 7077–7085.

[95] P. M. Allen, M. G. Bawendi, *J. Am. Chem. Soc.* **2008**, *130*, 9240–9241.

[96] G. Halder, S. Bhattacharyya, *J. Mater. Chem. A* **2017**, *5*, 11746–11755.

[97] M. A. Abate, J.-Y. Chang, *Sol. Energy Mater. Sol. Cells* **2018**, *182*, 37–44.

[98] H. I. Elim, W. Ji, M.-T. Ng, J. J. Vittal, *Appl. Phys. Lett.* **2007**, *90*, 33106.

[99] O. Yarema, M. Yarema, D. Bozyigit, W. M. M. Lin, V. Wood, *ACS Nano* **2015**, *9*, 11134–11142.

[100] P. Benoit, P. Charpin, R. Lesueur, C. Djega-Mariadassou, *Jpn. J. Appl. Phys.* **1980**, *19*, 85.

[101] I. D. Olekseyuk, O. V. Krykhovets, *J. Alloys Compd.* **2001**, *316*, 193–202.

[102] S. Chen, J. Chang, S. Tseng, L. Chang, J. Lin, *J. Alloys Compd.* **2016**, *656*, 58–66.

[103] V. P. Sachanyuk, G. P. Gorgut, V. V. Atuchin, I. D. Olekseyuk, O. V. Parasyuk, *J. Alloys Compd.* **2008**, *452*, 348–358.

[104] G. Delgado, A. J. Mora, C. Pineda, T. Tinoco, *Mater. Res. Bull.* **2001**, *36*, 2507–2517.

[105] R. S. Roth, H. S. Parker, W. S. Brower, *Mater. Res. Bull.* **1973**, *8*, 333–338.

[106] L. Tian, H. I. Elim, W. Ji, J. J. Vittal, *Chem. Commun.* **2006**, 4276–4278.

[107] N. D. Abazović, M. I. Čomor, M. N. Mitrić, E. Piscopiello, T. Radetić, I. A. Janković, J. M. Nedeljković, *J. Nanoparticle Res.* **2012**, *14*, 810.

[108] T. Bai, C. Li, F. Li, L. Zhao, Z. Wang, H. Huang, C. Chen, Y. Han, Z. Shi, S. Feng, *Nanoscale* **2014**, *6*, 6782–6789.

[109] M.-A. Langevin, A. M. Ritcey, C. N. Allen, *ACS Nano* **2014**, *8*, 3476–3482.

[110] L. Tian, M. T. Ng, N. Venkatram, W. Ji, J. J. Vittal, *Cryst. Growth Des.* **2010**, *10*, 1237–1242.

[111] W. Sun, S. T. Dacek, S. P. Ong, G. Hautier, A. Jain, W. D. Richards, A. C. Gamst, K. A. Persson, G. Ceder, *Sci. Adv.* **2016**, *2*, e1600225.

[112] S. Srinivasan, R. Batra, D. Luo, T. Loeffler, S. Manna, H. Chan, L. Yang, W. Yang, J. Wen, P. Darancet, S. Sankaranarayanan, *arXiv*, https://arxiv.org/abs/2004.08753v2, **2020**.

[113] A. O. Oliynyk, L. A. Adutwum, B. W. Rudyk, H. Pisavadia, S. Lotfi, V. Hlukhyy, J. J. Harynuk, A. Mar, J. Brgoch, *J. Am. Chem. Soc.* **2017**, *139*, 17870–17881.

[114] F. Legrain, A. van Roekeghem, S. Curtarolo, J. Carrete, G. K. H. Madsen, N. Mingo, *J. Chem. Inf. Model.* **2018**, *58*, 2460–2466.

[115] A. R. Oganov, C. J. Pickard, Q. Zhu, R. J. Needs, *Nat. Rev. Mater.* **2019**, *4*, 331–348.

[116] A. Swarnkar, A. R. Marshall, E. M. Sanehira, B. D. Chernomordik, D. T. Moore, J. A. Christians, T. Chakrabarti, J. M. Luther, *Science* **2016**, *354*, 92–95.

[117] S. Dastidar, C. J. Hawley, A. D. Dillon, A. D. Gutierrez-Perez, J. E. Spanier, A. T. Fafarman, *J. Phys. Chem. Lett.* **2017**, *8*, 1278–1282.

[118] L.-C. Xu, R.-Z. Wang, L.-M. Liu, Y.-P. Chen, X.-L. Wei, H. Yan, W.-M. Lau, *J. Mater. Chem.* **2012**, *22*, 21662–21666.

[119] S. Li, D. Pan, *J. Cryst. Growth* **2012**, *358*, 38–42.

[120] V. Zannier, T. Cremel, A. Artioli, D. Ferrand, K. Kheng, V. Grillo, S. Rubini, *J. Appl. Phys.* **2015**, *118*, 95702.

[121] T. Cremel, M. Elouneg-Jamroz, E. Bellet-Amalric, L. Cagnon, S. Tatarenko, K. Kheng, *Phys. Status Solidi C* **2014**, *11*, 1263–1266.

[122] S. Liu, Q. Zhang, L. Zhang, L. Gu, G. Zou, J. Bao, Z. Dai, *J. Am. Chem. Soc.* **2016**, *138*, 1154–1157.

[123] M. M. Richter, in *Opt. Biosens. Second Ed.*, Elsevier, Amsterdam, Netherlands, **2008**.

[124] L. Li, F. Tu, L. Jin, W. C. H. Choy, Y. Gao, J. Wang, *Sci. Rep.* **2014**, 4, 1–5.

[125] Q. Guo, S. J. Kim, M. Kar, W. N. Shafarman, R. W. Birkmire, E. A. Stach, R. Agrawal, H. W. Hillhouse, *Nano Lett.* **2008**, *8*, 2982–2987.

[126] L.-C. Xu, R.-Z. Wang, L.-M. Liu, Y.-P. Chen, X.-L. Wei, H. Yan, W.-M. Lau, *J. Mater. Chem.* **2012**, *22*, 21662–21666.

[127] S. B. Zhang, S.-H. Wei, A. Zunger, H. Katayama-Yoshida, *Phys. Rev. B* **1998**, *57*, 9642–9656.
[128] O. Yarema, M. Yarema, V. Wood, *Chem. Mater.* **2018**, *30*, 1446–1461.
[129] S. B. Qadri, E. F. Skelton, D. Hsu, A. D. Dinsmore, J. Yang, H. F. Gray, B. R. Ratna, *Phys. Rev. B* **1999**, *60*, 9191–9193.
[130] S. H. Tolbert, A. P. Alivisatos, *Science* **1994**, *265*, 373–376.
[131] P. Cottingham, R. L. Brutchey, *Chem. Mater.* **2018**, *30*, 6711–6716.
[132] R. Mainz, A. Singh, S. Levcenko, M. Klaus, C. Genzel, K. M. Ryan, T. Unold, *Nat. Commun.* **2014**, *5*, 3133.
[133] T. Hu, J. S. Wittenberg, A. M. Lindenberg, *Nanotechnology* **2014**, *25*, 415705.
[134] F. Shimojo, M. Aniya, *J. Phys. Soc. Jpn.* **2005**, *74*, 1224–1230.
[135] C. Xiao, J. Xu, K. Li, J. Feng, J. Yang, Y. Xie, *J. Am. Chem. Soc.* **2012**, *134*, 4287–4293.
[136] I. Rom, W. Sitte, *Solid State Ion.* **1997**, *101–103*, 381–386.
[137] A. K. Shukla, H. N. Vasan, C. N. R. Rao, *Proc. R. Soc. Lond. Ser. Math. Phys. Sci.* **1981**, *376*, 619–633.
[138] D. T. Schoen, C. Xie, Y. Cui, *J. Am. Chem. Soc.* **2007**, *129*, 4116–4117.
[139] J. Jang, F. Pan, K. Braam, V. Subramanian, *Adv. Mater.* **2012**, *24*, 3573–3576.
[140] K.-H. Nam, J.-H. Kim, W.-J. Cho, H.-B. Chung, *Appl. Phys. Lett.* **2013**, *102*, 192106.
[141] A. Sahu, A. Khare, D. D. Deng, D. J. Norris, *Chem. Commun.* **2012**, *48*, 5458–5460.
[142] A. Rogalski, J. Antoszewski, L. Faraone, *J. Appl. Phys.* **2009**, *105*, 91101.
[143] A. G. Abdullayev, R. B. Shafizade, E. S. Krupnikov, K. V. Kiriluk, *Thin Solid Films* **1983**, *106*, 175–184.
[144] S. Ithurria, P. Guyot-Sionnest, B. Mahler, B. Dubertret, *Phys. Rev. Lett.* **2007**, *99*, 265501.
[145] K. Jacobs, J. Wickham, A. P. Alivisatos, *J. Phys. Chem. B* **2002**, *106*, 3759–3762.

Author Biographies

Richard L. Brutchey began his independent career in 2007 at the University of Southern California where he is currently a Professor of Chemistry. The Brutchey group focuses on the design of inorganic materials to address challenges in catalysis, energy conversion and storage, and sustainability. His honors include being named a 2010 Cottrell Scholar and receiving the 2020 ACS Nanoscience Award. He has held appointments as a visiting professor at the Swiss Federal Institute of Technology Zürich in 2014 and as the Joseph Meyerhoff Visiting Professor at the Weizmann Institute of Science in 2021.

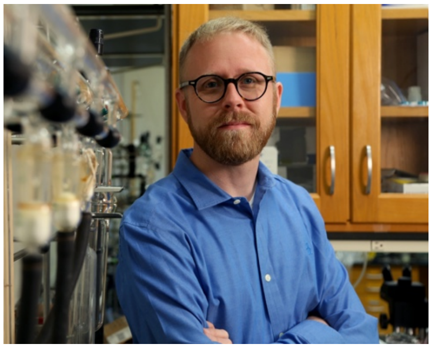

Bryce A. Tappan received a B.S. in Chemistry from the University of Kansas in 2016. He then joined the Brutchey group at the University of Southern California as a doctoral student. There, his primary research interests lie in the development of new synthetic techniques toward the predictable isolation of semiconductor nanocrystals with metastable crystal structures.

Frontispiece

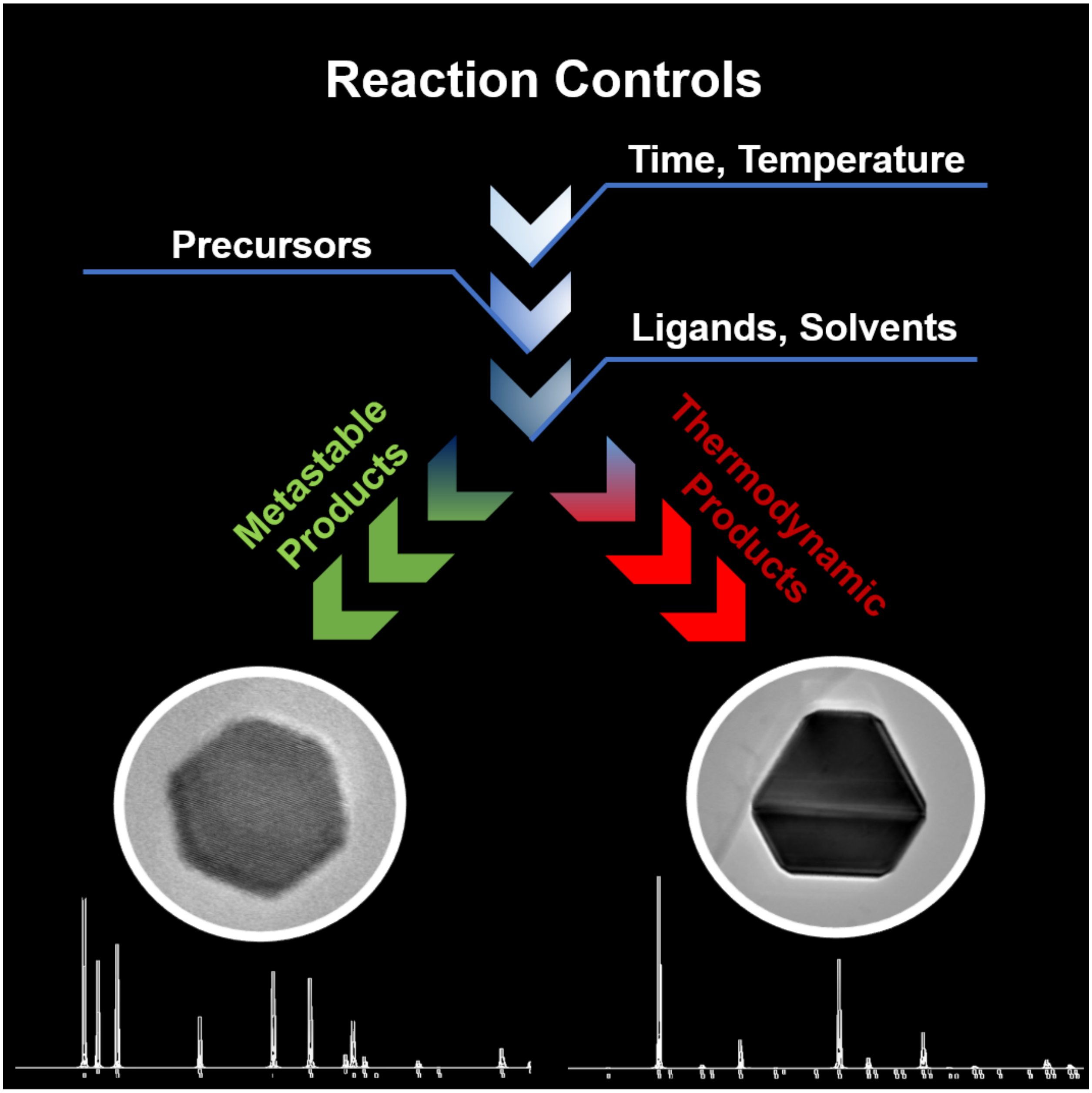
Reaction Controls
Time, Temperature
Precursors
Ligands, Solvents
Metastable Products
Thermodynamic Products